INFLUENCING HALIDE SEGREGATION IN PEROVSKITE NANOCRYSTALS VIA SURFACE TREATMENT

by

MICHAEL LYNN CRAWFORD

A DISSERTATION

Presented to the Department of Chemistry and Biochemistry
and the Division of Graduate Studies of the University of Oregon
in partial fulfillment of the requirements
for the degree of
Doctor of Philosophy

September 2022

DISSERTATION APPROVAL PAGE

Student: Michael Lynn Crawford

Title: Influencing Halide segregation in Perovskite Nanocrystals via surface treatment

This dissertation has been accepted and approved in partial fulfillment of the requirements for the Doctor of Philosophy degree in the Department of Chemistry and Biochemistry by:

Andy Marcus	Chair
Cathy Wong	Advisor
Ramesh Jasti	Core Member
Hailin Wang	Institutional Representative

and

Krista Chronister	Vice Provost for Graduate Studies

Original approval signatures are on file with the University of Oregon Division of Graduate Studies.

Degree awarded September 2022

DISSERTATION ABSTRACT

Michael Lynn Crawford

Doctor of Philosophy

Department of Chemistry and Biochemistry

September 2022

Title: Influencing Halide segregation in Perovskite Nanocrystals via surface treatment

Nanocrystals (NCs) of mixed-halide perovskite materials offer great potential for solar cells and light-emitting devices owing to their unusual defect tolerance and the tunability of their bandgap via size and halide composition. However, widespread adoption of these mixed-halide perovskite materials is prevented by bandgap instability due to segregation of the halides upon exposure to light or electrical current. This segregation creates regions with a narrower bandgap than the well-mixed phase, redshifting the emission spectrum. In this work I describe efforts to prevent this process by chemical treatment of methylammonium lead iodide-bromide ($MAPbI_xBr_{3-x}$) NCs using a mixture of small, strongly-binding ligands. I use transient absorption (TA) spectroscopy to collect dynamics information during halide segregation, informing a computational model used to extract mechanistic information about the halide segregation process. Using this model, I determine that the observed spectroscopic trends are best explained by iodide anions preferentially segregating into a region within the NC, rather than directly toward the NC surface. The mechanistic insight provided by this work will contribute to future approaches to stabilizing the bandgap in mixed-halide perovskite NCs.

CURRICULUM VITAE

NAME OF AUTHOR: Michael Lynn Crawford

GRADUATE AND UNDERGRADUATE SCHOOLS ATTENDED:

University of Oregon, Eugene, OR, USA
Illinois State University, Normal, IL, USA

DEGREES AWARDED:

Doctor of Philosophy, Chemistry, 2022, University of Oregon
Bachelor of Science, Chemistry, 2016, Illinois State University

AREAS OF SPECIAL INTEREST:

Perovskite Nanocrystals
Ultrafast Transient Absorption Spectroscopy
Computational Simulation of Nanocrystals

PROFESSIONAL EXPERIENCE:

Graduate Teaching Fellow, University of Oregon, 2016-2022
General Chemistry Lab Instructor, University of Oregon, August 2021

GRANTS, AWARDS AND HONORS:

Graduate Student Award for Excellence in Teaching of Chemistry, University of Oregon, 2021
Achievement Rewards for College Scientists Foundation, Oregon Chapter Scholar Award, University of Oregon, 2016-2019

PUBLICATIONS:

Crawford, M. L.; Sadighian, J. C.; Hassan, Y.; Sadhanala, A.; Snaith, H. J.; Wong, C. Y. Investigating Excited-State Dynamics in Mixed-Halide Lead Perovskite Nanocrystals. In Preparation.

Hassan, Y.; Park, J. H.; Crawford, M. L.; Sadhanala, A.; Lee, J.; Sadighian, J. C.; Mosconi, E.; Shivanna, R.; Radicchi, E.; Jeong, M.; Yang, C.; Choi, H.; Park, S. H.; Song, M. H.; De Angelis, F.; Wong, C. Y.; Friend, R. H.; Lee, B. R.; Snaith, H. J. Ligand-Engineered Bandgap Stability in Mixed-Halide Perovskite LEDs. *Nature* **2021**, *591 (7848), 72–77.*

Gordon, B. P.; Lindquist, G. A.; Crawford, M. L.; Wren, S. N.; Moore, F. G.; Scatena, L. F.; Richmond, G. L. Diol It up: The Influence of NaCl on Methylglyoxal Surface Adsorption and Hydration State at the Air–Water Interface. *J. Chem. Phys.* **2020**, *153 (16), 164705.*

Sadighian, J. C.; Wilson, K. S.; Crawford, M. L.; Wong, C. Y. Single-Shot Transient Absorption of Nascent Perovskite Nanocrystals. *The 22nd International Conference on Ultrafast Phenomena 2020* **2020**, Tu3A.6

Sadighian, J. C.; Wilson, K. S.; Crawford, M. L.; Wong, C. Y. Evolving Stark Effect During Growth of Perovskite Nanocrystals Measured Using Transient Absorption. *Front. Chem.* **2020**, *8, 585853.*

Sadighian, J. C.; Wilson, K. S.; Crawford, M. L.; Wong, C. Y. Understanding perovskite nanocrystal growth using in situ transient absorption spectroscopy. *Proc. SPIE 11464* **2020**, *Physical Chemistry of Semiconductor Materials and Interfaces XIX*, 114640K.

Sadighian, J. C.; Crawford, M. L.; Suder, T. W.; Wong, C. Y. Surface Ligation Stage Revealed through Polarity-Dependent Fluorescence during Perovskite Nanocrystal Growth. *Journal of Materials Chemistry C* **2020**.

Crawford, M. L.; Sadighian, J. C.; Hassan, Y.; Snaith, H. J.; Wong, C. Y. Spectral Shifts upon Halide Segregation in Perovskite Nanocrystals Observed via Transient Absorption Spectroscopy. *MRS Advances* **2020**, *5 (51), 2613–2621.*

Sadighian, J. C.; Crawford, M. L.; Wong, C. Y. Rapid Sampling during Synthesis of Lead Halide Perovskite Nanocrystals for Spectroscopic Measurement. *MRS Advances* **2019**, *4 (36), 1957– 1964.*

ACKNOWLEDGEMENTS

I thank my advisor, Cathy Wong, for her invaluable mentorship, abundant patience, thoughtful insight, and ready assistance in finding the best in a situation. Working with Cathy has helped me grow as a scientist, communicator, teacher, and mentor.

I thank everyone in the Wong lab for their friendship and help over the years. Each have taught me something new about research or teaching, for which I am grateful. In particular, I thank Martin Gruber and James Sadighian for their help in thinking about and executing experiments. Each have devoted many hours toward exploring what we can achieve together in the lab, and the results are something I think we can all be proud of.

The generous financial support of the ARCS Oregon Chapter is gratefully acknowledged. This work was partially supported by the National Science Foundation under Grant No. 1752129.

To my parents, whose encouragement to pursue higher education and whose support every step of the way have allowed me to do my best.

TABLE OF CONTENTS

Chapter Page

LIST OF FIGURES

LIST OF TABLES

Table Page

CHAPTER I

INTRODUCTION

In recent years, the reported efficiency of solar cells and light-emitting diodes fashioned from perovskite materials has skyrocketed. Nanocrystals (NCs) of perovskite materials offer great potential for these applications. In order to develop NCs for use in these applications, an understanding of the behavior of photoexcited electrons and holes is instrumental. In this work, I report on the evolving excited-state dynamics in perovskite NCs as they undergo the deleterious photoinduced segregation of halides within the crystal lattice, and how chemical treatment of the NC surface by tailored passivating ligands can avoid this problem. Halide segregation is described in detail in section 1.4.4. In this introduction, I first introduce features of NCs in general that inform my research study and methodology, followed by a discussion of perovskite materials and the problems addressed by this work.

1.1 NC Characterization Techniques

Absorbance and photoluminescence (PL) spectroscopies are easy and powerful techniques to characterize the behavior of perovskite NCs during synthesis and photoinduced halide segregation. When NCs absorb light, they form a bound electron-hole pair called an "exciton". NCs behave differently than bulk films, due to quantum confinement associated with their small size. Quantum confined structures including NCs are noted for the tunability of their band structure via size and composition.[1] NCs typically absorb across a broad spectrum extending from their excitonic absorption peak into the near-UV.[2] As the size of the NC increases, the absorbance onset and PL spectrum shift to redder wavelengths. The PL spectrum of many NCs can be easily discerned from among a mixture of

emissive materials, as they tend to emit strongly and within a narrow wavelength range.[2] Using this quality, it is possible to estimate NC size distribution using the PL spectrum, which is easily experimentally accessible without specialized equipment and can be quickly collected.

Absorbance and PL spectroscopies, while rich in the information they can provide, are limited to measurements of the ground state or states that are emissive after an arbitrary development time post-excitation. The behavior of the excited NCs as they relax over time is therefore missed by these techniques. This limitation can be defeated by using ultrafast time-resolved techniques, such as ultrafast transient absorption. Transient absorption spectroscopy is performed by first generating an excited population within a sample via absorption of a short "pump pulse", followed after some development time by a probe pulse whose transmission spectrum is measured. Transient absorption is a differential measurement, in that the results are reported as a difference in the transmission of the probe pulse through the excited sample vs a sample that has not been excited. The presence of charge carriers generated by the pump pulse can modulate the absorption spectrum of the sample at the arrival time of the probe pulse, leading to different observed effects in the spectrum. Further discussion of these effects, including possible insights they offer regarding the properties of the NC surface, is presented in Section 1.2.

For a more direct measurement of particle sizes, transmission electron microscopy (TEM) is frequently employed. This family of techniques works by imaging the NCs over space, offering atomic-resolution images and allowing for the evaluation of both the sizes and shapes of individual NCs. In this work, we have attempted to characterize NCs by these methods. However, these methods, while

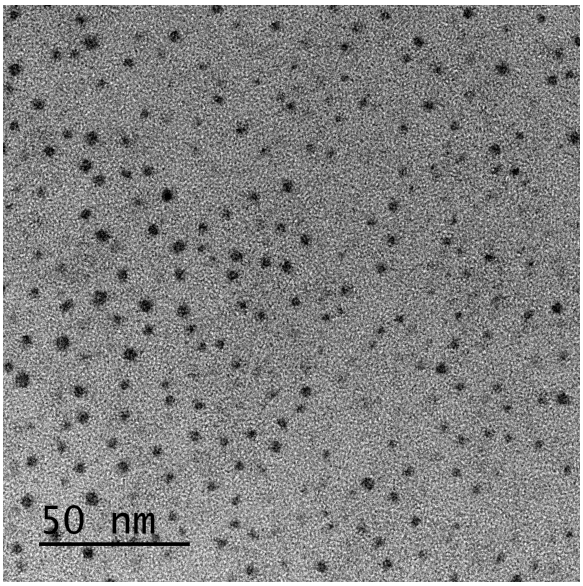

Figure 1. Example TEM image collected of NCs synthesized in this work. The signal to noise ratio is insufficient to determine trustworthy size distribution data.

powerful, present a challenge for characterizing perovskite materials due to their sensitivity to the electron beam.[3] The electron beam integral to these techniques can cause degradation of the perovskite crystal structure, initially by dissociating the surface ligands and halide anions.[4] In particular, hybrid organic-inorganic perovskite materials (e.g. $MAPbI_3$) are orders of magnitude more sensitive to the electron beam than all-inorganic perovskites (e.g. $CsPbI_3$), with a structural damage threshold as low as a total of tens of electrons per square angstrom. Because of this limitation, collection of useful images using conventional TEM instruments is extremely challenging, and our results were limited. A representative image we were able to collect via TEM is displayed in Figure 1. Here I will describe alternate TEM methods which may enhance future studies of individual perovskite NCs, including a method by which the ligands on the NC surface may be directly observed.

One alternate method to collect atomic resolution images is via direct detection of the transmitted electrons rather than detection of the light emission from a fluorescent film, allowing for much lower electron doses.[3] This technique was first utilized by Zhang et al. to image $MAPbBr_3$.[5] Another approach is to use integrated differential phase contrast TEM, which has allowed the use of a sufficiently low electron dose to successfully collect of images of $MAPbBr_3$ NCs with a spatial resolution of 1.5 angstroms.[3]

Specialized TEM techniques can also provide information about the ligands bound to the surface of the NC.[6] Collection of TEM images that offer information on the ligand shell is experimentally challenging, as it requires there to be good contrast between the atomic numbers of the atoms in the analyte and the atoms in the underlying support material, typically amorphous carbon. Panthani et al. successfully use graphene as the support material during TEM measurements, enabling the collection of images of silicon NCs with molecular resolution of the dodecene and octadecene ligands on the NC surface.[7] The repeating structure of the graphene support allows for the subtraction of its contribution to the collected images. This may offer a future pathway of characterizing ligand binding on the surfaces of NCs, which can have a large impact on the NC properties due to the large surface area to volume ratio. These techniques may be useful to further investigations into perovskite NCs and the development of their surfaces during growth or degradation.

Both spectroscopic interrogation of large populations of perovskite NCs and interrogation of individual NCs via spatially-resolved imaging techniques are invaluable methods of characterizing the behavior of NCs and unlocking their potential in practical applications. In the present work, PL and TA spectroscopies

are used to gain insight into the behavior of NCs during synthesis and after surface passivation with a tailored mixture of ligands. I discuss the use of surface ligands to modify the surfaces of NCs in section 1.4.3.

1.2 Electric Field Effect and Biexciton Binding Energy Observed in NCs Via Transient Absorption Spectroscopy

In this work, the most important technique utilized is TA spectroscopy. This spectroscopic technique is invaluable for characterizing the excited state dynamics in NCs, enabling the evaluation of the suitability for NCs for light emitting or absorbing applications. More details about the signals collected by this method are provided in Section 2.1.1.In this section I discuss two such effects that are broadly relevant in NCs: the quantum-confined electric field effect, and the biexciton binding energy.

The quantum-confined electric field effect occurs when a charge carrier, either the electron or hole, becomes trapped at the surface of the NC. In this event, the separation of the electron and hole creates an electric field within the NC.[8,9] The presence of an electric field can modulate the energy levels and affect a redshifting in the absorption spectrum, causing a differential absorption line shape that resembles the first derivative of the linear absorbance spectrum in CdSe[9] and perovskite NCs.[8,10] The requisite carrier trapping at the surface of the NC is predicted to occur due to unpassivated trap states at crystal defects. Therefore the observation of the quantum-confined electric field effect may be indicative of poor surface coverage by passivating ligands.

While the quantum-confined electric field effect can develop due to poor surface passivation, the effect of the presence of a pre-existing exciton on the energy required to generate another (i.e. the biexciton binding energy) is observed even in

well-passivated NCs. By this effect, we expect a redshift in the absorption spectrum of the NC, since the presence of the first photogenerated exciton will reduce the transition energy associated with the generation of the second exciton via stabilizing interactions.[11] This has been reported for various NCs in several places in the literature,[12–15] including for perovskite NCs.[16–19] The accurate identification of the contributions from both the biexciton binding energy and the quantum-confined electric field effect to the TA spectra of NCs during growth is important to my work presented in section 3.3.

1.3 Quantum Size Effects in NCs

The size of the NC plays a large role in the possible exciton dynamics and emission spectra of perovskite NCs. This is illustrated by comparing two studies of $CsPbX_3$ NCs. NCs of $CsPbBr_3$ of sizes larger than the Bohr radius during halide exchange reactions are reported by Darmawan et al.[20] They show that the NCs prior to halide exchange exhibit multiphoton emission, indicative of emissive states within the NC due to polaronic confinement. During the initial stages of halide exchange introducing iodide anions into the lattice, the multiphoton emission changed to single photon emission, indicating that the emissive transition from states within the NC were quenched. The emission changed back to multiphoton emission over time during the halide exchange reaction. They attribute this behavior to an initial state where the whole NC is bromide-rich and has room for multiple emissive regions. The introduction of iodide anions leads to energy transfer from the bromide-rich regions to the new iodide-rich region, which becomes the only emissive region. In this regime, only single photon emission is measured. As more and more iodide is introduced, there becomes room for multiple iodide-rich emissive sites, and multiphoton emission is restored. The emission behavior of

$CsPbBr_3$ NCs during halide exchange introducing iodide to the lattice was also measured by Yoshimura et al.[21] They report the absence of multiple emission wavelengths as halide exchange proceeds, indicating that the NC emits light as a single quantum-confined unit, rather than from various regions within the NC. The NCs interrogated in Yoshimura's report are much smaller than the NCs observed by Darmawan et al. in their similar study (average edge length of 7.5 nm vs 19.0 nm),[20] indicating that the transition between the $CsPbX_3$ NC behaving as one quantum-confined unit and the NC emitting from discrete locations within the NC lies between these sizes. These studies serve to emphasize that NCs of the size studied in Chapter III may exhibit behavior related to discrete locations within the NC, rather than the entire NC acting as one unit, informing our interpretation of observed TA spectra.

1.4 Perovskite NCs show promise for photonic applications

In this work, perovskite nanocrystals are examined during synthesis and during the photoinduced segregation of the halides within the lattice, discussed in section 1.4.4. Here the term "perovskite" refers to the crystal structure which shares its name with the natural mineral from which the structure was first discovered, $CaTiO_3$.[22] Compounds of this structure have the formula ABX_3, where A and B are cations and X are anions. This arrangement forms large cavities surrounded by eight octahedra defined by the X anions at their corners. These large cavities are occupied by the A cation, from where it is coordinated by twelve X anions. The interior of each octahedron is occupied by one B cation, coordinated by the surrounding six X anions at the corners of the octahedron. While minerals with this structure do exist on Earth's surface, they are of particular importance within the high-pressure environments that exist deep within terrestrial planets,

with $MgSiO_3$ and $CaSiO_3$ composing the major components of the Earth's lower mantle.[22,23] In the proceeding sections, I will discuss the applications of perovskite NCs in solar cells and LED devices and problems preventing their widespread adoption.

1.4.1 Advantageous features of perovskite materials. Particular interest has recently been directed toward perovskite materials for photonic applications, with rapid development in photovoltaic applications since the first experiments toward this application in 2009.[24] Perovskite LEDs emissive at colors throughout the visible spectrum are accessible by tuning the size and halide composition of the NCs.[25] Thus they are promising for applications requiring a wide variety of band gaps. The positions of the band edges in lead halide perovskites are dictated by the lead ions and halide ions, while the A-site cation does not participate in the electronic structure of the band edges.[26] The A-site cation only indirectly influences the band gap, by stabilizing or distorting the lattice shape via the size of the ion. The upper valence band is formed from the halide outer p orbitals, while the lower conduction band is formed from unoccupied 6p orbitals of lead atoms.[27] It is reported that this band structures makes lead halide perovskites intrinsically defect tolerant due to the presence of molecular anti-bonding orbitals near the valence band maximum and bonding orbitals at the conduction band minimum.[28] This configuration, which is the opposite of the typical configuration in traditional semiconductor materials, reportedly serves to drive defect-induced states into either the conduction band or the valence band, rather than within the band gap where deleterious charge trapping would result.[29–31] However, there are some calculations reported that predict the presence of some small concentration of deep electron traps due to halide vacancies.[32]

Overall, the tolerance of the perovskite lattice to defects without forming deep trap states is promising for their use in practical applications.

The bandgap tunability and defect tolerance exhibited by perovskite NCs have lead to intense research into their application into both solar panels and LED devices. With advances in tuning the halide and cation compositions of the NCs, a power conversion efficiency of up to 17.39% is reported for devices composed of layered $Cs_{0.25}FA_{0.75}PbI_3$ with $CsPbI_3$.[33] Meanwhile, perovskite LEDs emissive at colors throughout the visible spectrum are accessible by tuning the size and halide composition of the NCs. In 2016, Deng et al. reported LEDs made by dip-coating solutions of methylammonium lead halide quantum dots, with blue, green, and red emission wavelengths accessible by varying the halide composition.[34] They report that the use of NCs rather than bulk films enhances the efficiency of the device by avoiding the long diffusion lengths characteristic of perovskite films. This promising feature of NCs over bulk films motivates the investigations in this work.

1.4.2 Challenges preventing widespread adoption. One of the challenges associated with using perovskites in practical applications is their poor stability when exposed to water vapor, oxygen, heat, and sunlight.[35–37] These sensitivities present an important challenge to the widespread adoption of perovskites for photonic applications, as their fast degradation makes them unappealing for large-scale commercial adoption. The use of perovskite NCs can serve to help avoid these sensitivities and unlock practical applicability. In 2021, my colleagues and I reported the characterization of an LED from $MAPbI_xBr_{1-x}$ NCs with an external quantum efficiency of 20.3%, which is within the range of commercial organic LED devices.[38] This efficiency was obtained by treating the surfaces of the NCs with a mixture of ethylene diamine tetraacetic acid (EDTA)

and L-glutathione ligands. The effects of surface ligands on proprieties of the NC will be discussed in section 1.4.3. The rapid development of devices with efficiency that competes with commercially-available devices within just a few years illustrates how promising the next few years may be for perovskite NC LEDs.

One of the reasons that perovskite materials can be unstable under typical operating temperatures is the thermodynamics associated with transitions between their crystal phases. The presence of multiple crystal phases was noted even during the earliest reports of the syntheses of perovskite materials, when it was noted that $CsPbBr_3$ would form white crystals that turn orange upon heating to 140°C.[39] The crystal structure of these materials with the most appropriate bandgap for solar applications is cubic, sometimes called the "black phase" or "α phase".[35,40–42] This phase is not thermodynamically favorable at room temperature. Instead, other phases are favored at typical operating temperatures.[43] For example, in $CsPbI_3$, the α phase is not favored until a temperature as high as 320°C, with another phase referred to as the δ phase being favored at room temperature.[44] This effect also exists for perovskites using formamidinium and methylammonium at the A-site.[45] However, this effect can be avoided via the use of NCs rather than bulk material. It has been reported that the surface energy associated with the high surface area to volume ratio of NCs stabilizes the α phase, even at ambient temperatures.[41,44,46] This indicates that wide-scale commercial viability may be enhanced by the use of NCs rather than bulk films.

However, even if the α phase is stabilized, perovskite materials which use methylammonium at the A-site suffer from additional temperature-induced loss of organic gas and therefore collapse of the perovskite crystal structure.[36,47] To avoid this temperature-induced degradation, alternate cations can be employed at

the A-site, including formamidinium, cesium, and small quantities of rubidium.[48] Because the main function of the A-site cation is to stabilize the cubic phase of the lattice via filling the cavities between the lead halide octahedra, a certain minimum size is required to fulfill this role. Most metal cations are too small, and are thus precluded from this use. It is instructive to consider the difference between cesium and rubidium ions to find a threshold size for consideration. While the difference in the ionic radii between rubidium and cesium may seem small (152 pm and 167 pm, respectively) rubidium cannot be used as the sole A-site cation within the lattice, as it is too small to support an α phase at any temperature on its own.[49] By substituting methylammonium for formamidinium, or organic cations for inorganic cations, device cell stability can be improved. In particular, devices which incorporate mixtures of cations have demonstrated good stability.[50]

Another key sensitivity of perovskite materials is to water vapor. The effects of water are complicated,[37] with humidity during synthesis reported to improve crystallinity,[51,52] film formation,[53–55] and photoluminescence.[52,56] At the same time, humidity has been reported to degrade perovskite films over time, requiring encapsulation against the ambient environment during fabrication and use of perovskite devices.[57–59] Avoiding degradation due to environmental factors is paramount to the widespread adoption of perovskite materials in mainstream light emitting and absorbing devices. Thus, efforts to improve their stability are ongoing. It has been reported that moisture-initiated degradation has been avoided by encapsulating the perovskite material by various chemical means, including encapsulation with a polymer shell[60] and the use of "water-proof" molecules as surface ligands during synthesis of NCs.[61]

1.4.3 Surface Defect Passivation via Surface Ligation.

Quantum-confined structures, including NCs, exhibit properties that are strongly dependent on their surface conditions due to their extremely high surface area to volume ratio.[6,62,63] Most device applications require the defect density in the material to be quite low, since defects can form deep trap states within the band gap, trapping carriers and obstructing either charge transfer or radiative recombination processes.[28] An illustration of shallow and deep trap states is displayed in Figure 2. Shallow trap states are those near the band edges within the band gap, reversibly trapping the electron or hole. Defects are particularly frequent at the surfaces of NCs, as there is less strain there preventing defect formation.[6] It has been shown that recombination events predominantly occur via states where either the electron or hole is localized at the surface in CdS,[64] CdSe,[9,65] and perovskite NCs.[66] It is therefore necessary to consider the characteristics of the surfaces of the NCs for a proper understanding of their behavior. In this work, the impact of treating the NC surface with small, strongly-binding ligands is investigated, and in particular the ability of these ligands to prevent the formation of surface trap states is observed.

The impact of surface traps can be avoided by chemically treating the surface. Passivating the NC surface with ligands can both reduce the impact of surface traps and enhance the stability of NCs in solution.[28,67,68] One way to describe the binding of ligands to the surface of NCs is called Covalent Bond Classification, proposed by Green et al. in 1995.[69] Broadly, this model describes three different ways ligands can bind to a metal atom: X-type ligands, which bind to a metal atom using one electron to form a two-electron covalent bond; L-type ligands, which bind by donating two electrons to an empty orbital on the metal

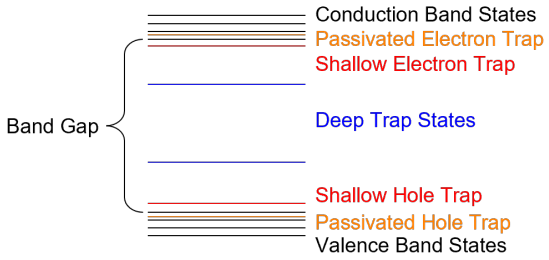

Figure 2. Illustration of the different states discussed in the text. Upon photoexcitation, an electron will exist in the conduction band while a hole will exist in the valence band, and each particle may become reversibly trapped in shallow trap states, or irreversibly trapped in deep trap states. Trapping prevents charge transport, which is integral to the operation of photovoltaic devices, and encourages nonradiative recombination, reducing the efficiency of light-emitting devices. With passivation via the binding of surface ligands, the energies of these states can be adjusted to lie within the conduction or valence bands, keeping the band gap "clean".

atom; and Z-type ligands, which bind to a metal atom by accepting a pair of electrons from the metal into an empty orbital. L-type ligands behave as Lewis bases, binding to available lone pairs on the NC surface, while Z-type ligands behave as Lewis acids and bind to available vacant orbitals on the NC surface.[70] In these regimes, ligands can act to passivate the NC surface and avoid the development of trap states within the band gap by binding to dangling bonds or vacancies at the NC surface. It has been shown that the energy difference between shallow trap states and the band edges in $CsPbBr_3$ NCs depends on the surface ligands.[71] In Chapter III, I discuss the utilization of a mixture of small, strongly-binding ligands at NC surface to prevent the occurrence of halide segregation.

1.4.4 Halide Segregation. While the band gap of perovskite materials can be tuned via halide composition, narrowing of the band gap during device operation due to spontaneous segregation of the halides within the lattice remains a difficult problem. The capacity to tune the band gap of these materials

via halide composition cannot contribute to the adoption of these materials if the resulting tailored band gap spontaneously narrows during use. Much of this work is devoted to avoiding halide segregation via chemical treatment of the NC surface. In this section, I will discuss the spectroscopic signatures of halide segregation, followed by a summary of proposed mechanisms. The discussion in Chapters III and IV of this work aims to contribute to the current understanding of the mechanism of halide segregation.

1.4.4.1 Spectral signatures of halide segregation. Spontaneous band gap narrowing was first observed in $MAPbI_xBr_{1-x}$ films in 2015 by Hoke et al.[72] They observed that the PL spectrum of their films redshifted over time when exposed to light, and that the spectrum partially recovered when the film was stored in the dark. This effect was assigned to segregation of iodide anions into local iodide-enriched domains, supported via the development of XRD peaks indicative of the formation of iodide-rich (approx. 70% iodide) and bromide-rich (approx. 20% iodide) domains. The halide composition within the NC plays a defining role in determining the band gap in the material, since the valence band energy is largely dictated by the halide orbitals. Iodide 6p orbitals lead to a higher valence band edge than bromide 5p or chloride 4p orbitals.[27] Photogenerated excitons relax to iodide-rich regions within the lattice due to the lower energy of the band edges in those locations, causing the observed redshifting of the emission spectrum.

Spatially-resolved techniques have confirmed that halide segregation is associated with photoinduced band gap narrowing. While it has been known since the initial report of halide segregation that grain boundaries are not required for halide segregation,[72] these spatially-resolved techniques have shown that iodide-

rich regions preferentially form at surfaces and grain boundaries within films. The first spatially-resolved indications were reported by Bischak et al., who used cathodoluminescence imaging to reveal the formation of iodide-enriched regions along grain boundaries within $MAPbI_{0.3}Br_{2.7}$ films after exposure to 405 nm light.[73] Using computational models, they show that a high degree of electron-phonon coupling is required to cause halide segregation. The presence of iodide-rich regions at grain boundaries was further confirmed by Shao et al.,[74] who used conductive atomic force microscopy at locations near and far from grain boundaries to characterize the band gap at those locations. They show that ion migration is much faster at grain boundaries in $MAPbI_3$ films, due to the lower activation energy for iodide migration there. This effect suggests that halide segregation occurs faster with smaller grain sizes, which makes this effect of paramount importance for NCs. The characteristics of the NC surfaces are therefore of particular concern for the studies presented here.

Much of the contribution in this work centers on the impact of the surface on the process of halide segregation. We have previously shown that some TA signals can report on the characteristics of the NC surface.[8,75] One of the features on the NC surface that can contribute to TA signals is the existence of electron or hole traps on the surface. The interaction of electrons and holes with these states is important to an overall understanding of the relaxation processes within NCs, as well as informing the mechanism assigned to halide segregation. To better understand the kinetics of charge carrier trapping and detrapping, one study used time-resolved fluorescence upconversion (FLUPS) of $CsPbBr_3$ NCs paired with TA to determine kinetics of trapping and detrapping.[71] The FLUPS decay contains a fast component not present in the TA spectrum, attributed by the authors to

reversible trapping of the exciton in dark shallow trap states. The authors use a kinetic model, along with the assumption that the transition energy between the dark trap states and the band edge is less than the available thermal energy to determine the rates of trapping and de-trapping of the charge carriers. The authors confirm by this model that the observed difference between the FLUPS and TA dynamics is explainable by reversible trapping of the exciton. This study serves to emphasize that the relaxation kinetics of perovskite NCs may include contributions from many discrete states whose populations evolve over time, necessitating careful interpretation. This may also suggest that trap states at the NC surface contribute to the reported buildup of iodide there.

1.4.4.2 Effect of halide segregation on relaxation kinetics.

TA spectroscopy can offer rich dynamics information on the relaxation processes in NCs. Using this method, several groups have sought to determine how the transfer of charge carriers to iodide-rich regions impacts the recombination kinetics in perovskite materials. In one study comparing TA of bulk films of $MAPbI_3$ and $MAPbBr_3$, it is reported that the TA signals in the bromide film decay faster than those in the iodide film.[76] The Auger recombination rate is particularly sensitive to halide composition, proceeding four times faster in $MAPbBr_3$ than in $MAPbI_3$.

Observing the TA kinetics in $MAPbI_3$ and $MAPbBr_3$ individually misses the impact of the interactions between iodide-rich and bromide-rich regions when they exist in the same perovskite lattice. Multiple groups report that mixed-halide films exhibit faster decay in signals attributed to bromide-rich regions than those attributed to iodide-rich regions. This can be attributed to electrons and holes in bromide-rich regions preferentially transferring to iodide-rich regions where the band gap is narrower.[77,78] These studies serve to emphasize that the excited

state dynamics in mixed-halide systems such as those studied in this work may show complex interactions that must be carefully interpreted. In section 3.2, I report finding that the relaxation kinetics of $MAPbI_2Br$ NCs speeds up after halide segregation

TA spectra have been reported in the literature of $MAPbI_xBr_{3-x}$ thin films before and after halide segregation.[77,78] The formation of iodide-rich regions within these films is associated with the formation of a sub-band gap bleach feature in the TA spectrum, as well as a speeding up of the kinetics associated with bromide-rich regions. This speeding up is attributed to the new relaxation pathway provided by transfer of charge carriers from bromide-rich regions to iodide-rich regions. I report in Chapter III measurements of the overall redshifting of the TA spectra from $MAPbI_xBr_{3-x}$ NCs after halide segregation, accompanied by an overall speeding up of the relaxation kinetics. In Chapter IV I seek to explain this speeding up of the relaxation kinetics using a computational model that tracks the iodide anions throughout the NC over time during halide segregation. In using this computational model, we are able to evaluate the ability of our TA data to support proposed mechanisms of halide segregation.

1.4.4.3 Proposed mechanisms of halide segregation. One aim of the present study is to contribute to the discussion on the mechanism of halide segregation in perovskite NCs. In this section, current proposed mechanisms are detailed for later comparison to spectroscopic evidence collected in this work and discussed in Chapters III and IV.

In order for halide segregation to occur, the process of halides migrating between sites within the crystal lattice must have a sufficiently low activation energy. Halide mobility through the perovskite crystal lattice is mediated by

crystal defects, which are predicted to be present in significant quantities at room temperature in $MAPbI_3$.[79] It has been shown computationally that iodide vacancy migration in $MAPbI_3$ has a lower activation energy than the migration of the other ions (0.58 eV, versus 0.84 eV for the methylammonium cation and 2.31 eV for the lead (II) cation).[80] This lower activation energy grants the iodide anion an estimated diffusion coefficient four orders of magnitude higher than migration of the methylammonium cation, allowing iodide to migrate significant distances at room temperature. Experimental evidence has established that halides in the perovskite lattice are quite mobile, even sufficiently mobile to exchange between films when they are placed in physical contact. This effect was demonstrated by Elmelund et al., who created mixed-halide perovskite films by using binder clips to press films of $MAPbI_3$ and $MAPbBr_3$ together.[81] This extent of mobility supports the notion that halide segregation is a plausible explanation for the observed band gap narrowing.

With confirmation that halides are mobile within the perovskite lattice, the precise mechanism of halide segregation may be considered. Several mechanisms of halide segregation characterized by strain-mediated effects have been proposed. Any proposed mechanism would have to explain: (1) some mechanism that assigns different activation energies to iodide and bromide anions migrating into a certain region, (2) the re-mixing of the halides in the dark, and (3) the role of surfaces and grain boundaries in attracting iodide rather than bromide anions. Any proposed mechanisms involving crystal surfaces are supported by computational studies, wherein the authors showed that the formation energy of iodide vacancy and interstitial defects is reduced at the $MAPbI_3$ perovskite surface,[82] and that interstitial iodide defects tend to migrate toward crystal surfaces.[83]

Hoke et al. initially proposed a mechanism by which photogenerated holes are trapped by randomly preexisting iodide-rich regions, causing local strain which is stabilized by the migration of more iodide toward the trapped hole.[72] After recombination, this strain is relieved and entropic effects lead to halide remixing. This mechanism was later built upon by Bischak et al., who proposed that photoinduced halide segregation occurs when photogenerated charges induce strain within the lattice via the strong electron-phonon coupling observed in $MAPbI_xBr_{3-x}$ materials.[73] The photogenerated polarons migrate to preexisting random iodide-enriched locations and stabilizes them, becoming trapped in the process. Recombination therefore occurs from within iodide-rich regions, and photoexcitation encourages the development of these regions. During continued illumination, the iodide-rich regions are stabilized by polarons over time and tend to migrate toward the crystal surface. After illumination is stopped, it is entropically favorable for the halides to remix.

An alternate halide segregation mechanism involving the activity of the surface is proposed by Belisle et al.[84] in an attempt to explain results showing that uneven illumination may be a prerequisite for halide segregation in bulk films.[77] According to their model, the action of electron-donating surface ligands forms a shell of partially positively-charged ligands at the perovskite surface. Upon illumination, this layer of positive charge attracts photogenerated electrons from deeper in the bulk of the lattice toward the illuminated surface. The buildup of electrons at the surface attracts positive lattice defects toward the surface, and drives negative defects into the bulk. As the formation of bromide vacancies has a lower associated activation energy than the formation of iodide vacancies, the

buildup of positive defects at the illuminated surface amounts to a net migration of bromide deeper into the lattice.

The buildup of charge at the perovskite surface has been implicated by another proposed mechanism by Chen et al.[85] Upon observing that the development of iodide-enriched phases is fastest near the edges and corners of their mixed-halide microplatelets, they propose a mechanism based upon the large carrier diffusion rate in perovskite materials. The diffusion of charge carriers leads to a build-up of carrier density near the crystal surfaces since the surfaces act as a "dam" past which the carriers cannot diffuse. This large carrier density causes a build-up of strain in regions near the surfaces, which is relieved by the accumulation of iodide anions.

Despite these insights, is unclear which mechanism or effect is most descriptive of the process of halide segregation in NCs. In this work, I use transient absorption spectroscopy to seek mechanistic insight into halide segregation in NCs. As discussed in Chapter III, the TA signals collected in this work before and after halide segregation are globally fit to reveal the evolving excited-state dynamics. These results are used in Chapter IV to inform a computational model of evolving halide distribution within NCs over time.

1.5 NC Growth Mechanisms

Historically, the synthesis of NCs has been guided by the mechanism proposed by LaMer in 1950.[86,87] Under this regime, NC nucleation occurs in a "burst" after sufficient precursor has dissolved to supersaturate the reaction solution. After the initial burst, further dissolved precursors contribute toward the growth of existing nuclei, rather than creating additional nuclei. This mechanism

was initially proposed for the formation of sulfur NCs, without the impacts of coordinating ligands or multiple precursors considered.

The first instance of perovskite NCs grown in solution was reported in 2014 by Schmidt et al.[67] By their reprecipitation method, NCs of $MAPbBr_3$ are synthesized by reacting MABr with $PbBr_2$ in a mixture containing oleic acid and medium- and long-chain alkylammonium bromide ligands dissolved in octadecene. The precipitation of the NCs is initiated by the injection of acetone, an anti-solvent, into the reaction vessel. In the presence of these ligands, the authors propose that NCs are isolated by this method because the long-chain alkylammonium bromide ligands prevent the aggregation of the NC cores. By this method, perovskite NCs can be grown quickly, easily, and from inexpensive starting materials. A similar method was later developed by Hassan et al., in which $MAPbI_3$ and $MAPBI_2Br$ NCs were synthesized by injection of a mixture of perovskite precursors dissolved in a compound solvent of acetonitrile/methylamine into a solution of capping ligands in toluene, an anti-solvent.[88]

These methods are each very fast to produce fully-formed NCs, within seconds to minutes. The reaction conditions, including temperature and atmospheric humidity and oxygen content, must be finely controlled to achieve desired NC properties.[89] A much slower synthesis that can operate under ambient conditions is demonstrated by Wang et al.[89] In this method, hereafter referred to as the solvation-mediated synthesis, the precursors are suspended in a nonpolar solvent along with dissolved capping ligands. The ligands act to solvate the precursor material, after which nucleation and NC growth occur. By this method, the final NC size can be controlled by allowing the NCs to grow for some duration of time, then quenching NC growth by removing the solid precursor material. With

the solids removed, the NCs no longer gain more material over time, and they stop growing. NCs of $MAPbI_3$, $MAPbBr_3$, and $MAPbI_xBr_{3-x}$ are reported.

My colleagues and I have further investigated the mechanism of synthesis during the solvation-mediated synthesis of $MAPbI_3$ NCs.[75] We discerned via PL spectroscopy of several samples during synthesis of $MAPbI_3$ NCs that the NC surfaces are not well-capped by the ligands in solution during the initial stages of growth, but rather the NCs become well-capped after the NCs have been growing for 15 minutes. The reasons behind this behavior are not currently understood.

The solvation-mediated synthesis technique still has several open questions regarding the precise mechanism of NC growth, especially as applied to mixed-halide NCs. For example, it is not know whether the mixed-halide NCs have a constant halide composition throughout growth, or whether they start off rich in one with the other doping into the lattice over time. It has also not been shown that the surface coverage of mixed-halide NCs evolves over time in the same way that we have observed for $MAPbI_3$. These mechanistic insights would be invaluable for tuning of the NC properties by tailored synthetic conditions.

CHAPTER II

METHODS

The description of single-shot transient absorption in section 2.1.2 was adapted from co-authored work in which Dr. Kelly Wilson developed the described instrumental setup, while James Sadighian and I performed the described experiments. The co-authored material is published in:

> Sadighian, J. C.; Wilson, K. S.; Crawford, M. L.; Wong, C. Y. Evolving Stark Effect During Growth of Perovskite Nanocrystals Measured Using Transient Absorption. *Front. Chem.* **2020**, *8*, 585853.

The content in section 2.1.3 includes co-authored material in which I described the experimental setup I designed and applied in this work. The co-authored material is published in:

> Crawford, M. L.; Sadighian, J. C.; Hassan, Y.; Snaith, H. J.; Wong, C. Y. Spectral Shifts upon Halide Segregation in Perovskite Nanocrystals Observed via Transient Absorption Spectroscopy. *MRS Advances* **2020**, *5* (51), 2613–2621.

2.1 Instrumental Methods

2.1.1 Transient Absorption Spectroscopy. Ultrafast TA spectroscopy is a pump-probe technique that uses femtosecond pulses to generate an excited population in a sample and measure its absorption spectrum after a range of delay times. The instrumental setup is depicted in Figure 3. We use a Ti:Sapphire laser source that outputs 800 nm laser pulses (red line in Figure 3) at a rep rate of 1 kHz and with a pulse duration of around 40 fs. This pulse is split into pump and probe pulses. The pump pulse is directed through an optical parametric amplifier which converts the wavelength of the pulse to a desired wavelength, here 520 nm (green line in Figure 3). The pump pulse is then directed through a prism

compressor setup, which adds a tailored amount of negative dispersion to the pulse such that it is as short in duration as possible at the sample plane, 40-100 fs. Meanwhile, the probe pulse is focused into a white light generation medium, either sapphire or argon. This converts the wavelength spectrum of the probe pulse into a broad continuum, gray line in Figure 3, via the method discussed in Section 2.1.2. The transmission of the probe pulse through the sample is measured at each wavelength using a CMOS camera.

TA signal is reported as the difference in the transmission of the probe pulse through the sample before and after the sample is excited by the pump pulse. In the simplest case, the following formula could be used:

$$\frac{\Delta T}{T} = \frac{T_{\text{with pump}} - T_{\text{without pump}}}{T_{\text{without pump}}} \tag{2.1}$$

where $T_{\text{with pump}}$ and $T_{\text{without pump}}$ are the measured transmission when the pump pulse is and is not allowed to excite the sample, respectively. In this simplest case, the transmission without the pump is measured by periodically blocking the pump pulse using an optical chopper tuned to 500 Hz. This frequency blocks every other pulse. The ΔT/T signal is recorded as a function of wavelength and time delay between the arrival of the pump and the probe. To access different time delays, the path length of one of the pulses is changed using a retroreflector on an automated motorized delay stage.

Further background subtraction is pursued by adding a second chopper to the setup in the path of the probe pulse, tuned to 200 Hz. This creates four kinds of exposures on the camera: an exposure where neither pulse is blocked, an exposure where the pump is blocked, an exposure where the probe is blocked, and an exposure where both pulses are blocked. The exposure with the probe blocked is used to account for the contribution of any fluorescence from the sample or scatter

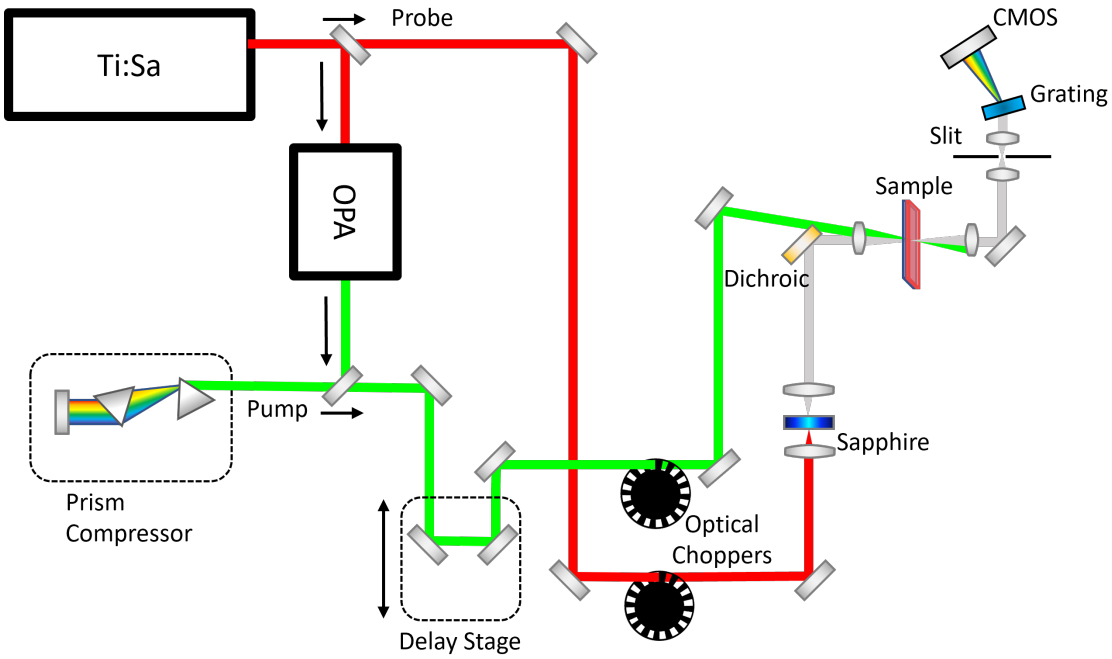

Figure 3. Diagram of TA instrument. Depicted are the 800 nm laser from the Ti:Sapphire source (red), the 520 nm pump pulse generated by the optical parametric amplifier (green), and the broad-spectrum probe pulse generated via supercontinuum generation (gray) and reflected off a dichroic mirror which transmits the unconverted 800 nm intensity.

of the pump pulse off of anything within the setup. The exposure with both pulses blocked is used as a background, allowing for the subtraction of the electric dark and any ambient light around the room which might reach the CMOS. These exposures are combined according to the following formula to isolate just the ΔT/T signal:

$$\frac{\Delta T}{T} = \frac{(T_{\text{pump and probe on}} - T_{\text{pump on probe off}}) - (T_{\text{pump off probe on}} - T_{\text{pump and probe off}})}{(T_{\text{pump off probe on}} - T_{\text{pump and probe off}})} \tag{2.2}$$

By this method, the excited state dynamics is measured as a function of wavelength and time delay. The TA signals are recorded using the CMOS and custom software developed by Dr. Kelly Wilson for our lab.

2.1.1.1 TA Signals. There are three kinds of signals that can be observed using TA spectroscopy: excited-state absorption (ESA), stimulated emission (SE), and ground state bleach (GSB). These signals are depicted diagrammatically in Figure 4 and described here. While considering these signals, it is helpful to remember that, according to the definition in equation 2.1, if more light makes it to the detector due to the excitation of the sample, then a positive signal will be observed. Likewise, if less light makes it to the detector due to the excitation of the sample, a negative signal will be observed.

ESA occurs when excited NCs absorb a photon to reach some higher excited state. This absorption causes fewer photons to reach the detector, producing a negative ΔT/T signal. SE occurs when an incident photon can stimulate an emissive transition within the NC to release another photon toward the detector. This causes more photons to reach the detector, visible as a positive ΔT/T signal. GSB is a decrease in the absorptivity of the sample at certain wavelengths due to

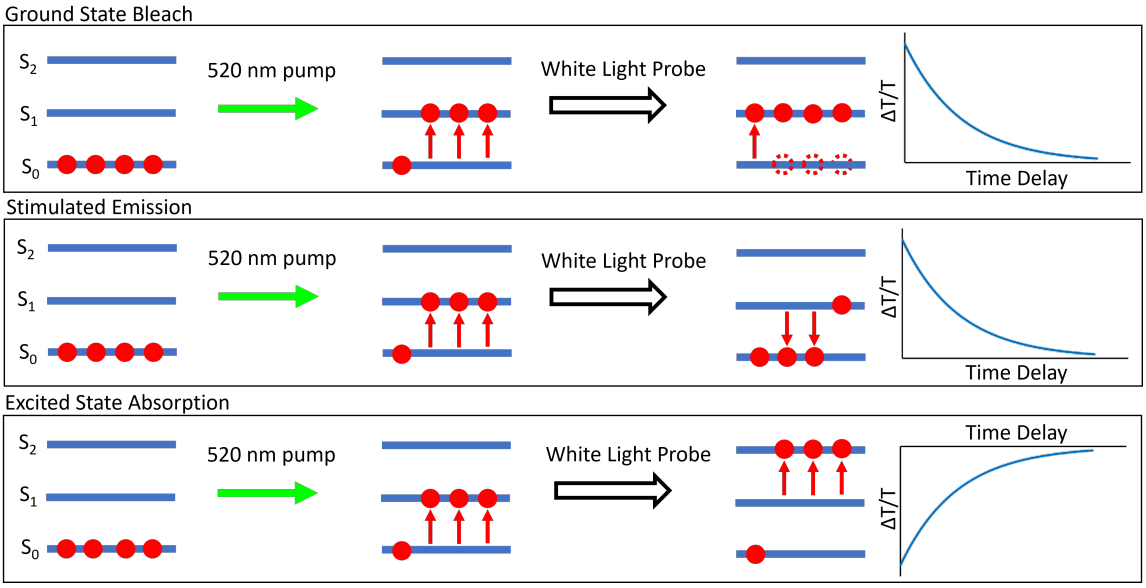

Figure 4. Diagram of TA signals described in the text. Ground state bleach (GSB) arises due to the depopulation of the absorptive ground state, yielding a positive $\Delta T/T$ contribution. Stimulated emission (SE) is observed when probe photons stimulate the an emissive transition in the sample, yielding a positive $\Delta T/T$ contribution. Excited state absorption (ESA) is observed when the photogenerated excited population further absorbs light to reach higher excited states, yielding a negative $\Delta T/T$ contribution.

the depopulation of the absorptive ground state. This causes more photons to reach the detector, visible as a positive ΔT/T signal.

The ΔT/T signal is monitored as a function of wavelength and pump-probe time delay. It is typical to extract two kinds of information from the signals: dynamical and spectral. The dynamical information can tell us how the electronic state of the excited sample evolves over time, while spectral information can tell us about the energy of the transitions between the available electronic states. Interpretation of TA signals can be complicated because different relaxation processes within the sample happening in concert can contribute different signals over the same range of wavelengths. To help disambiguate our interpretation, fitting of the TA signals is usually required.

In my work, I fit the TA signals to a sum of k exponential functions:

$$\frac{\Delta T}{T}(\lambda, t) = \sum_{n=1}^{k} A_n(\lambda) \exp \frac{-t}{\tau_n} \tag{2.3}$$

For a dataset with m discrete wavelengths, each exponential function contains $m + 1$ fitting parameters: m $A_n(\lambda)$ parameters and one τ_n, for a total of $k(m + 1)$ degrees of freedom in the fit. The parameters τ_n serve as the time constant for each exponential. Because τ_n is not a function of wavelength, these fitting parameters impact only the dynamics information within the fit signal. The parameters $A_n(\lambda)$ serve as a wavelength-dependent amplitude. Because $A_n(\lambda)$ is not a function of time, these parameters impact only the spectral information in the fit signal. Using this method, I have seen success in extracting spectral and dynamical information from TA signals. For an example of how this method is used to interpret TA results, see Chapter III.

2.1.2 Single-Shot Transient Absorption. During TA experiments using a traditional setup such as depicted in Figure 3, transients are typically

collected by physically moving a retroreflective mirror to vary the path length of the pump or probe pulse, thereby varying the relative arrival time of the pulses at the sample. The $\Delta T/T$ signal is measured across the interrogated wavelength range at each retroreflector position. This iterative process of moving the retroreflector and collecting TA signal necessitates a relatively long period of data collection, during which time a sample could degrade or evolve, frustrating the characterization of the sample. Samples that evolve faster than TA signals can be collected are therefore inaccessible to traditional TA spectroscopic apparatus.

The collection of TA signals is streamlined using the single-shot transient absorption (SSTA) spectrometer built for our lab. In this instrument, the pump and probe pulses are focused to lines using cylindrical lenses. The pump pulse is directed toward the sample at an angle, causing one side of the sample to be excited sooner than the other side, as depicted in Figure 5. The probe pulse is then transmitted through the sample normal to its surface and is directed to a detector.

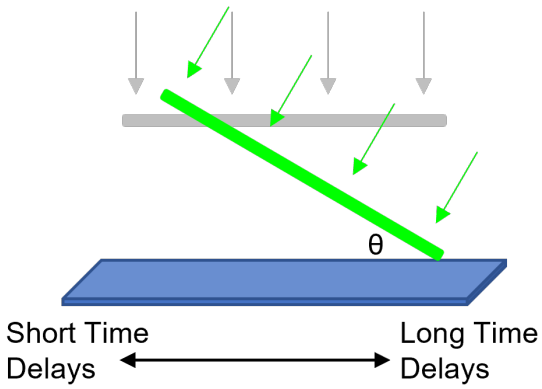

Figure 5. Diagram of the probe (gray) and pump (green) pulses as they approach the sample during a single-shot transient absorption experiment. The pump pulse arrives at the right side of the sample sooner than the left side, allowing the right side to develop for a longer time delay duration before the probe pulse reaches the sample. The illuminated length of the sample and the angle between the pump and the sample (θ) determine the accessible time delay range.

One weakness of this SSTA approach is that the time delay range accessible during the experiment depends on the length of the illuminated region:

$$t_d Range = \frac{d \sin(\theta)}{c} \tag{2.4}$$

where c is the speed of light, d is the length of the illuminated region, and θ is the angle between the pump pulse and the sample, marked in Figure 5.[90] By this formula, under our instrumental setup which uses a pump angle of 52.5°, the sample must be uniform over at least a distance of 22 mm to access a full 60 ps time delay range. It can be difficult to prepare uniform films of this size in any material, and in particular the films provided to me by my collaborators were squares of side length 1 cm. With a 1 cm illuminated region, this would only allow for a time delay range of approximately 25 ps, making it impossible to measure longer time delays without moving the retroreflector. However, the required size of the sample is less of a problem for samples in the liquid state, which can quickly and easily be inserted into a cuvette of sufficient size to access the full 60 ps of time delay range. We apply SSTA to track the excited state dynamics in NCs at various times during the synthesis method described in Section 2.2.2. The collected SSTA data is summarized in Section 3.3.

2.1.3 Transient absorption / photoluminescence apparatus. For our samples whose sizes are too small to effectively apply the SSTA technique, a different method was required to expediently collect TA and fluorescence spectra during a single experiment. I developed a traditional TA setup that uses three laser beams incident upon one spot on the surface of the film. The configuration of the beams is depicted in Figure 6. Halide migration could generally be induced by the pump pulse, and was otherwise ensured by exposing the sample to a 405 nm CW laser for a chosen duration of time at a fluence of approximately 0.21 W cm^{-2}.

During exposure to the 405 nm laser, fluorescence was collected via an optical fiber (Thorlabs M53L01) placed in front of and above the sample, coupled into an Ocean Optics Flame-T spectrometer. TA was collected using a 520 nm pump pulse and a broad-spectrum probe pulse generated using the setup depicted in Figure 3, using 2 mm sapphire window as the white light generation medium. The pulses were overlapped spatially with each other and the 405 nm CW beam.

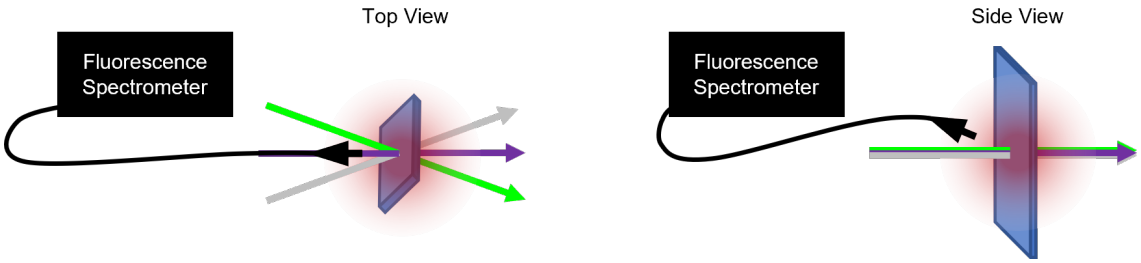

Figure 6. Schematic diagram of instrumental apparatus for collecting fluorescence and TA spectra of the NC film. TA is measured before and after the initial migration process using probe (gray) and pump (green) pulses. The 405 nm CW laser (purple) was incident on the sample (blue rectangle) during the initial migration process and during each subsequent exposure, during which fluorescence (red) was collected using an optical fiber (black) placed in front of the sample, above the plane of the beams.

TA was collected prior to illuminating the sample with the 405 nm laser, with the pump pulse typically inducing halide segregation. To ensure that any halide segregation or remixing that occurs during a TA scan is not systematically encoded into the transient, measurements were first conducted at alternating pump-probe time delay values in increasing order, followed by the remaining time delay values in decreasing order. The fluence of the 520 nm pump (4.2 μJ cm^{-2}) and broadband probe (5.4 μJ cm^{-2}) were not always sufficient to induce halide segregation. After collecting TA for one hour, the pump and probe beams were blocked, and the sample was exposed to the 405 nm laser for a variable duration of time in an attempt to ensure halide segregation would occur. During this time,

fluorescence was continuously monitored. We resumed collecting TA immediately after exposure to the 405 nm laser.

After halide segregation was ensured by exposure to the 405 nm laser, the collection of post-segregation TA signals requires that the sample remain segregated. It is widely reported in the literature that halide anions spontaneously re-mix when perovskite samples are left in the dark.[73,77,78,81,91] To mitigate the impact of this remixing, it is necessary to periodically re-expose the film during the TA data collection. This is accomplished by collecting TA for one minute, and then pausing the collection of TA data for some duration of time while the sample is re-exposed to the 405 nm laser and fluorescence is monitored. Then the 405 nm laser is again removed, and TA measurement is resumed. The fluorescence spectrum measured at the end of the initial exposure is compared to the fluorescence spectra measured during each subsequent re-exposure.

2.1.4 Supercontinuum generation in various media. During transient absorption measurements, it is required to have a source of broad-spectrum light pulses that are on the order of femtoseconds long. It is not possible to modulate the output of traditional broad-spectrum light sources, such as tungsten filaments, to such a short pulse. Instead, the process of supercontinuum generation is used. In this section, I will describe the process of supercontinuum generation mathematically.

Consider a laser pulse with a Gaussian wave envelope:

$$\begin{aligned} A &= I(t)\cos(\psi) \\ \psi &= kz - \omega t \\ I(t) &= I_0 \exp\left(-t^2/\tau^2\right) \end{aligned} \tag{2.5}$$

where A is the amplitude of the electric field, ψ is the phase of the light wave, ω is the frequency of the wave over time, k is the angular wave number, z and t are position in space and time, respectively, $I(t)$ is the intensity of the Gaussian wave envelope, I_0 is the maximum of the Gaussian wave envelope, and τ is the width of the Gaussian wave envelope. Here we consider one specific location z within the supercontinuum generation medium. The angular wave number can be substituted for the following:[92]

$$k := \frac{2\pi}{\lambda} = \frac{\omega_0 n(I)}{c} \tag{2.6}$$

where ω_0 is the angular frequency of the input laser pulse. This substitution allows for the expression of the phase in terms of the angular velocity:

$$\psi = \frac{\omega_0 n(I)}{c} z - \omega_0 t \tag{2.7}$$

This shows that the phase of the wave depends upon the index of refraction in the material it is propagating through. This can introduce time dependence due to the optical Kerr effect, the dependence of the index of refraction in a material upon the intensity of light propagating through it. The changing index of refraction is dependent upon $I(t)$ in the following way:[93]

$$\frac{dn(I)}{dt} = \frac{d}{dt} n_0 + \frac{d}{dt} n_2 I(t) \tag{2.8}$$

Where n_0 is the linear index of refraction, and n_2 is the second-order nonlinear index of refraction. Because n_0 and n_2 are constant values, the first term in Equation 2.8 is equal to zero. The remaining term is found by the following:

$$\frac{dn(I)}{dt} = \frac{d}{dt} n_2 I(t) = n_2 \frac{d}{dt} I(t) = n_2 \frac{d}{dt} I_0 \exp\left(-t^2/\tau^2\right) \tag{2.9}$$

$$\frac{dn(I)}{dt} = n_2 \frac{-2tI_0}{\tau^2} \exp\left(-t^2/\tau^2\right) \tag{2.10}$$

The changing of the index of refraction, described in Equation 2.10 introduces a change in the phase of the pulse, ψ. With the construction of ψ in equation 2.7, it becomes possible to determine the time-derivative of ψ:

$$\frac{d\psi}{dt} = \frac{d}{dt}\frac{2\pi\omega_0 n(I)}{c}z - \frac{d}{dt}\omega_0 t \tag{2.11}$$

$$\frac{d\psi}{dt} = \frac{2\pi z\omega_0}{c}\frac{d}{dt}n(I) - \omega_0 \tag{2.12}$$

$$\frac{d\psi}{dt} = \frac{2\pi z\omega_0}{c}n_2\frac{-2tI_0}{\tau^2}\exp\left(-t^2/\tau^2\right) - \omega_0 \tag{2.13}$$

Using Equation 2.13, we can solve for the frequency, which from equation 2.5 is equal to $-d\psi/dt$, as a function of time:

$$\omega(t) = -\frac{d\psi}{dt} = \omega_0 + \frac{2z\omega_0 n_2 I_0}{c\tau^2}t\exp -t^2/\tau^2 \tag{2.14}$$

By Equation 2.14, it is seen that the frequency of an input pulse of sufficient intensity will experience a redshift on the rising edge of the pulse and a blueshift on the falling edge.[94,95] The impact of this time-dependent frequency shift on the wavelength of the pulse is displayed in Figure 7.

Self-phase modulation is accompanied by its spatial counterpart, self-focusing. As a Gaussian pulse propagates through a medium and induces local intensity-dependent changes in the index of refraction, the difference in the index of refraction between the center and edges of the pulse act like a focusing lens, causing the pulse to narrow over space.[96] This focusing causes the pulse to become more intense toward its center, enhancing both the self-phase modulation and self-focusing effects. The self-focusing continues until competing defocusing effect of the generated plasma causes a nearly steady beam profile.[97] The pulse then propagates through the medium over long distances with a small profile, a phenomenon called

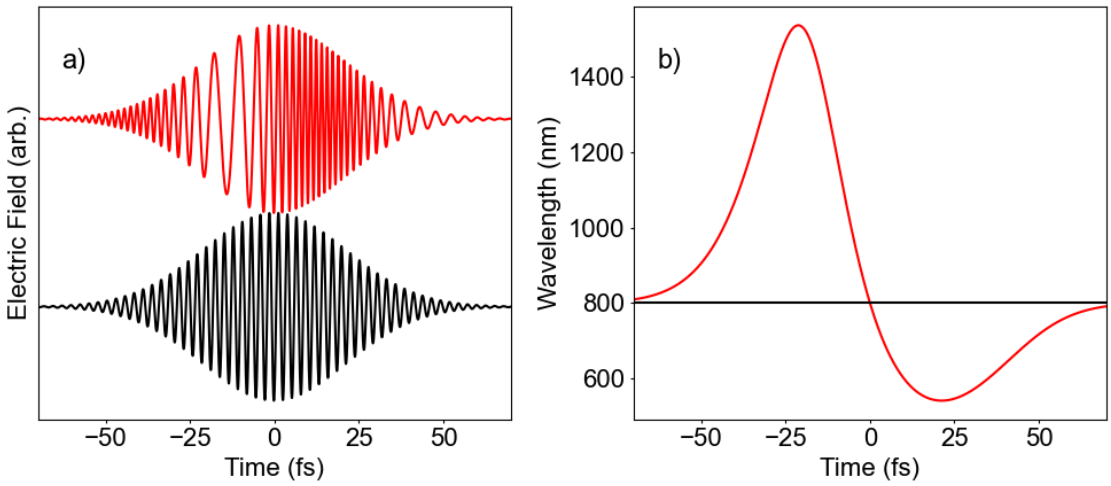

Figure 7. a) Sample 800 nm pulse input before (black) and after (red) self-phase modulation. The values of the linear and nonlinear indices of refraction and the distance within the medium were arbitrarily chosen such that the impact on the pulse is easily visible. b) The instantaneous wavelength of the pulse before (black) and after (red) self-phase modulation. The leading edge of the pulse (at negative times) is redshifted, and the falling edge of the pulse (positive times) is blueshifted.

"filamentation". This filamentation can be observed over relatively long distances through optical media.[98]

During the course of this project, I explored the use of several optical media as the supercontinuum generation medium, including sapphire, CaF_2, BaF_2, and argon. Representative white light spectra from each medium are compared in Figure 8. Out of those tested, sapphire was the only medium that did not produce intensity into UV wavelengths, which has also been observed by other groups.[99]

We observed that CaF_2 and BaF_2 crystals were damaged by the laser pulse within short durations of time, sometimes showing visible damage during a single TA experiment. I attempted to avoid laser-induced damage by using a homemade motorized translation stage to move the crystals. However, the crystals still accumulated damage over time, and the translation of the crystals allowed for the

damage to take place over much wider areas, as is visible in Figure 9. Media that are less susceptible or immune to laser-induced degradation, including sapphire and argon, are therefore more easily applicable long-term. During my experiments, I used sapphire as the generation medium for traditional TA measurements, whereas argon was chosen for SSTA measurements as it is not damaged at the high pulse energies employed for those experiments.

2.2 Preparing NCs

2.2.1 Synthesizing via LARP. The mixed-halide NCs studied in this work were synthesized by my collaborators via a ligand-assisted reprecipitation technique they developed, which I will briefly detail here.[88] By their method, NCs are created quickly upon addition of a precursor solution containing MAI, MABr, and PbI_2 dissolved in acetonitrile to a flask containing a solution of oleic acid and oleylamine in toluene. The toluene acts as an anti-solvent causing the immediate formation of NCs. These NCs are then purified by centrifugation and resuspension in toluene. Some volume of these NCs were reserved, while an aliquot was treated by stirring with EDTA and L-Glutathione powders overnight. NCs from each batch were then spin-cast into films and encapsulated between layers of glass. These samples were studied using PL and TA spectroscopies, as reported in Section 3.1.

2.2.2 Synthesizing via solvation-mediated technique. In order to slow down the synthesis of perovskite NCs so as to allow for multiple SSTA measurements during synthesis, a different method was implemented. This method, reported by Wang et al., relies on ligands dissolved in a nonpolar solvent to bind to the precursor materials, solvating them and allowing the reaction to proceed.[89] The precursors themselves are insoluble in nonpolar solvents, and so their interaction is mediated by their solvation by the ligands. By this method, NCs are synthesized in

solution under ambient conditions over the course of approximately two hours. We have used this method to prepare $MAPbI_3$, $MAPbBr_3$, and $MAPb(Br/I)_3$ NCs.

During a typical synthesis, 1 g of PbI_2 and 1 g of MAI are weighed into a vessel and set aside. A vial is charged with 20 mL of hexane, 20 μL of oleic acid, and 40 μL of octylamine. The vial of liquid is fitted with a floating collar and suspended in a temperature-controlled sonication bath. The solid precursors are then added to the vial and a timer is started. The vibration provided by the sonication bath is sufficient to continuously stir the system, creating a circulating suspension of the solid precursors in the ligand solution.

At chosen times throughout the synthesis, aliquots of the suspension can be withdrawn from the middle of the vial using a plastic syringe. Prior to spectroscopic measurements, it is required that the precursor particles are removed. This can be achieved by centrifuging the aliquot. However, centrifugation takes on the order of minutes to complete, over which time the NCs in the aliquot could be evolving in unknown ways. Rather than centrifuging the aliquot, we instead opt to filter it through a filter of nonpolar material, poly-tetrafluoroethylene (PTFE, "teflon"). It was found that this filtration quenches the reaction, allowing a spectroscopic characterization of the NCs as they exist in the solution at the time they are withdrawn.[75]

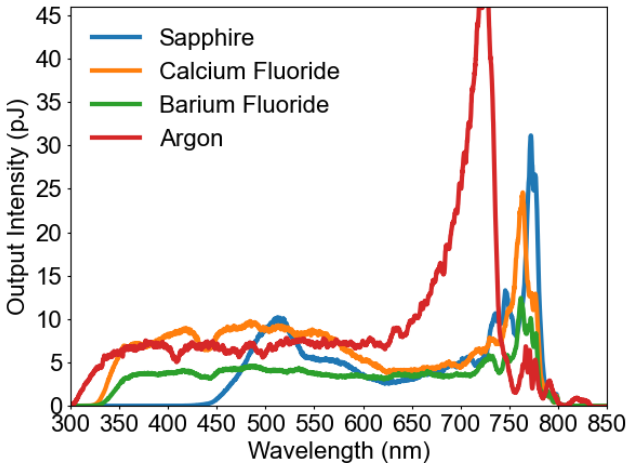

Figure 8. Representative white light spectra generated by focusing a short 800 nm pulse into several media. These spectra were collected after reflecting the output pulse off a dichroic mirror which transmits light at wavelengths longer than 800 nm, preventing the unconverted intensity at 800 nm from overloading the detector.

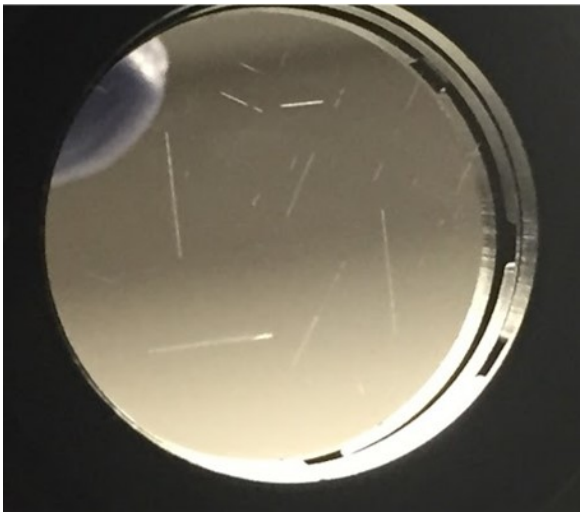

Figure 9. Photograph of the CaF_2 crystal after multiple supercontinuum generation experiments. While the crystal was translated in an attempt to avoid damage from the high intensity of the input laser pulses, the induced damage was spread over wider areas, producing the "scratches" visible in this photograph.

CHAPTER III

SPECTROSCOPIC RESULTS

This chapter includes co-authored material from work in preparation in which I present and discuss the results included in this chapter.

3.1 Effect of Surface Ligands on Photoluminescence

Luminescence redshifting due to halide segregation is an important problem for any application of mixed-halide perovskite species. Mitigation strategies focused on surface modification are good candidates for stabilizing NC systems, for which the surface area to volume ratio is very high. To this aim, we investigated $MAPbI_2Br$ NCs whose surface was treated with small, strongly-binding ligands: ethylenediamine tetraacetic acid (EDTA) and L-glutathione. The small size of these ligands allows for greater surface coverage than is possible with larger ligands, and the strength of their binding to the NC prevents them from desorbing and allowing halide segregation to proceed.

While these ligands were chosen for their potential to bind to the surface, their ability to strongly bind to Pb^{2+} cations also lead to the loss of some material from the NC. Our collaborators have found that treating NCs with either EDTA or L-glutathione rather than a mixture of the two caused the PL to increase in intensity and blueshift slightly.[38] The blueshift is correlated with a decrease in NC size after ligand treatment, indicating a loss of material. This is likely due to the ligands binding to Pb^{2+} cations and removing them from the NC. This blueshift and increase in intensity was also present when using a mixture of EDTA and L-glutathione, but using the two ligands together provides additional synergistic effects. Our collaborators used DFT calculations to determine that the EDTA and L-glutathione ligands interact with each other while bound to the NC

surface, mutually increasing their binding energy, thereby increasing their ability to passivate the NC surface and prevent halide segregation.[38]

PL spectra measured during exposure to the 405 nm migration laser are displayed in Figure 10. A large overall redshifting is observed in the PL spectrum of the untreated NC film, which is widely reported in literature to accompany halide segregation.[72] This effect is seen to a much lesser extent in the PL of the treated NC film, indicating that halide segregation is reduced after treatment with EDTA and glutathione. This indicates that the ligand treatment mitigates the bandgap instability that accompanies halide segregation in NCs. These spectra confirm that we are able to replicate the PL redshift associated with halide segregation. More information that can be used to determine the mechanism of halide segregation is collected via transient absorption spectroscopy. This technique was used to investigate the behavior of photoexcited electron-hole pairs over time before and after halide segregation.

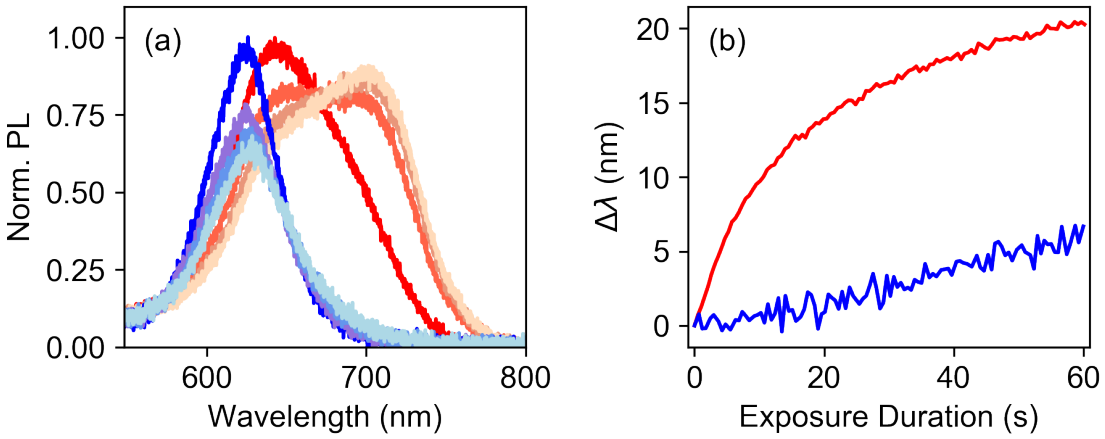

Figure 10. a) PL spectra of films without (red) and with (blue) ligand treatment after 0 s (darkest), 20 s, 40 s, and 60 s (lightest) of exposure to migration laser. b) The change in the average emission wavelength of NC films without (red) and with (blue) ligand treatment during the initial exposure to the migration laser.

3.2 Transient Absorption Shows Changing Exciton Dynamics Due to Surface Ligation

While the untreated NCs exhibit the significant PL redshift expected during halide segregation,[72] this effect is suppressed in the treated NCs, Figure 10, in agreement with our previous result.[38] This difference is also observed in TA. The TA spectrum comprises a bleach feature centered at 625 nm with excited state absorbance at higher and lower energies. While TA scans before exposure to the migration laser did not cause the bleach of treated NCs to redshift, redshifting was observed for nine of the 12 spots measured on the untreated NC film. The bleach signal for the remaining three spots redshifted upon exposure to the migration laser. Figure 11a,c show TA spectra of untreated NCs before and after exposure to the migration laser. The bleach redshift for the treated NCs after exposure to the migration laser is much smaller, Figure 11b,d.

Dynamics information is extracted from the TA signals using global fitting analysis, as described in Section 2.1.1.1. Here we fit the TA signals to the sum of four exponential functions with wavelength-dependent amplitude:

$$\frac{\Delta T}{T}(\lambda, t) = \sum_{n=1}^{4} A_n(\lambda) \exp \frac{-t}{\tau_n} \tag{3.1}$$

where t is the time delay between the arrival of the pump and the probe at the sample, λ is the wavelength, τ_n are wavelength-independent time constants, and $A_n(\lambda)$ are wavelength-dependent amplitudes. We were able to obtain good fits for these TA signals by using one exponential for the fast hot carrier cooling, and three exponential functions to describe the longer dynamics. Comparisons of global fitting results to the input TA data are displayed in Figure 12 and Figure 13. Fit time constants for the data displayed in Figure 11 are listed in Table 1.

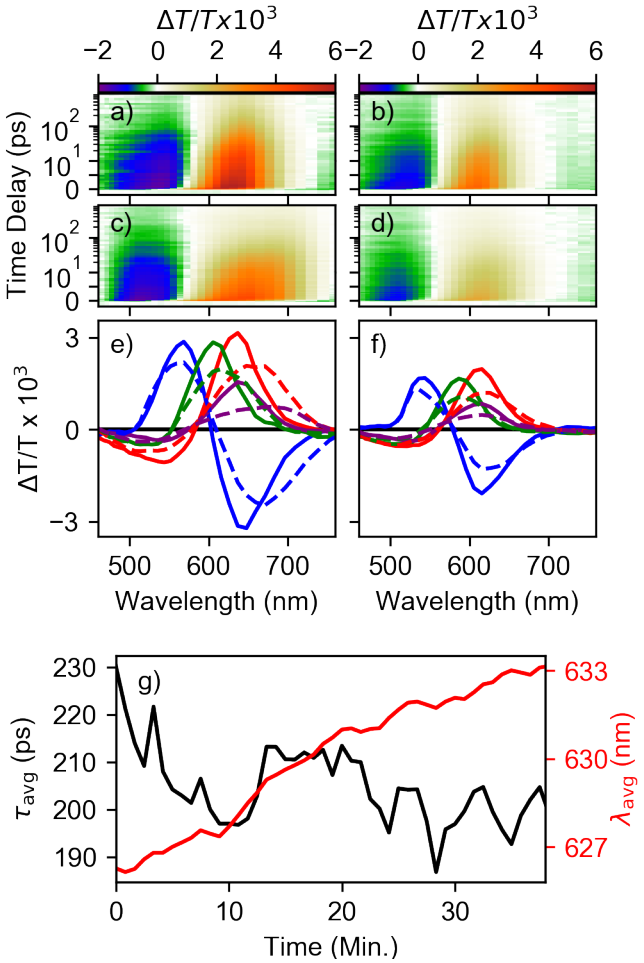

Figure 11. NC dynamics prior to halide segregation are represented by the average of (a) the first 25 TA scans of the untreated NCs and (b) 72 TA scans of the treated NCs. Average of one hour of TA scans on the same spots after exposure to migration laser for (c) untreated and (d) treated NCs. (e) Global fits of untreated NC spectra in (a) and (c) in solid and dashed lines, respectively. (f) Global fits of treated NC spectra in (b) and (d) in solid and dashed lines, respectively. Blue lines are spectra associated with the fast component and green, red, and purple lines are spectra associated with exponential components with increasing time constants. (g) The weighted average time constant from the global fits of untreated NCs at spots where exposure to TA pump pulse caused halide segregation, calculated using a 25-scan rolling average (black). This time constant trends downward, indicating that recombination dynamics speed up with halide segregation. Concurrently, the average wavelength of positive amplitude in the longest three exponentials redshifts (red).

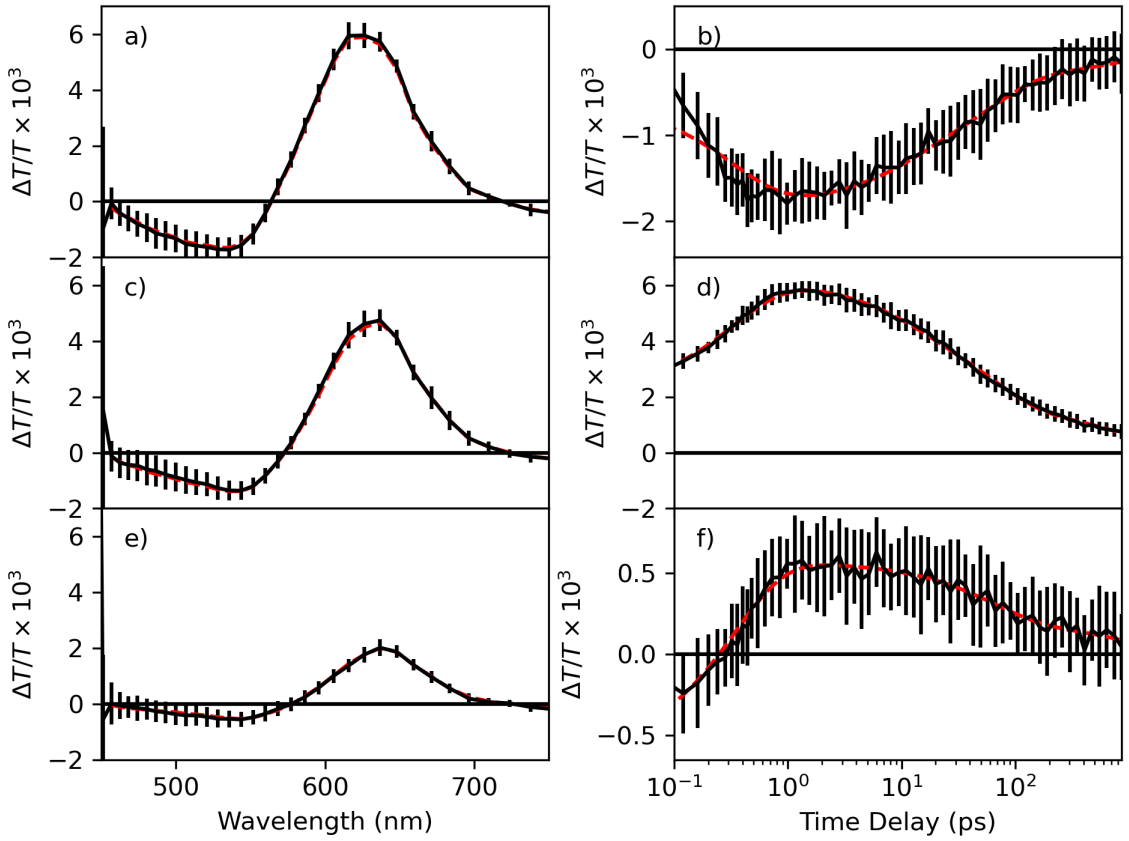

Figure 12. Global fit (dashed red) to TA signal (black) averaged over 12 spots on the film without ligand treatment. Error bars indicate the standard deviation of the signal collected during the first 25 scans, before halide segregation could impact the signal. In the wavelength domain are plotted TA spectra at 76.8 fs (a), 10.9 ps (c), and 105 ps (e). Transients are shown at 528 nm (b), 637 nm (d), and at 696 nm (f).

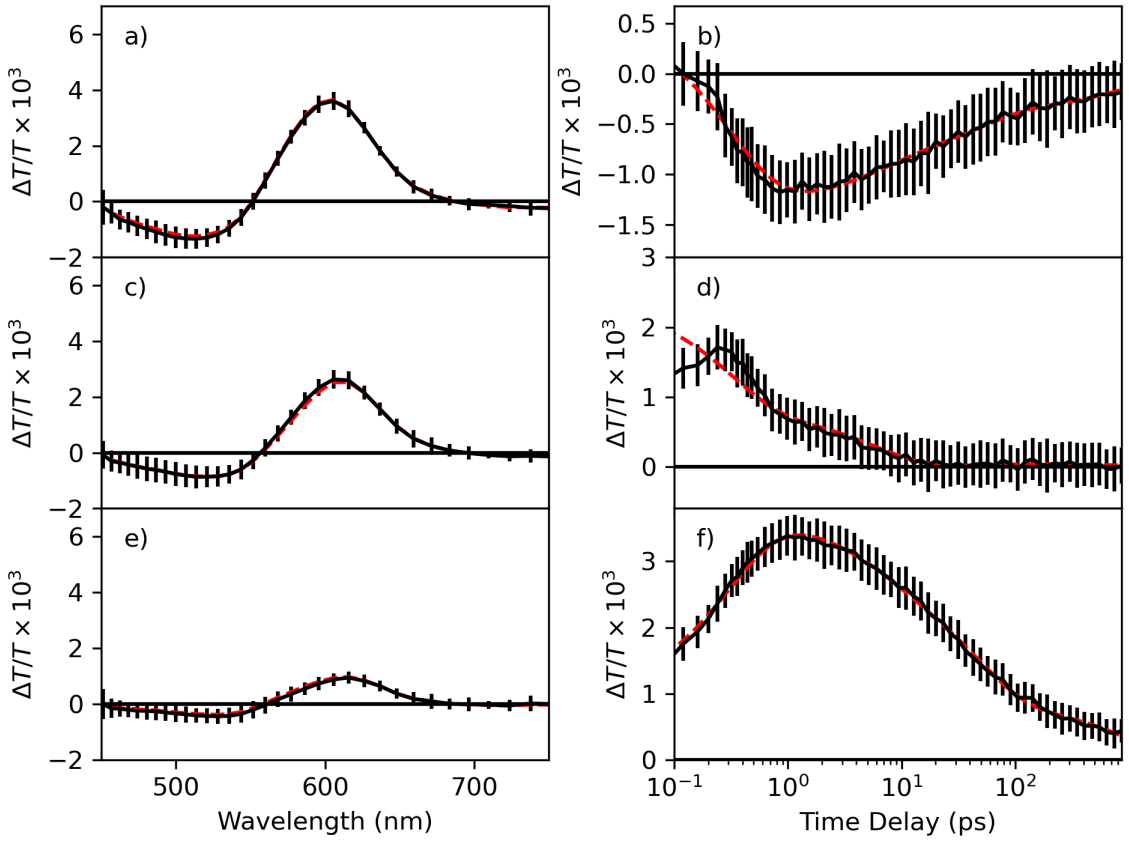

Figure 13. Collected TA spectra and dynamics for the TA data averaged at 13 spots on the film with ligand treatment before exposure to the migration laser. Collected TA signal is shown in black, with error bars indicating the standard deviation of the signals collected during 72 consecutive scans. The corresponding global fitting results are shown by dashed red lines. In the wavelength domain are plotted TA spectra at 76.8 fs (a), 10.9 ps (c), and 105 ps (e). The error bars become larger as the time delay increases, corresponding to the lower overall signal intensity after long relaxation times. In the time domain are plotted transients at 528 nm (b), 560 nm (d), and at 616 nm (f). Good agreement is noted between the fit and the observed TA spectra.

	Untreated film, first 25 TA scans	Untreated Film, one hour Post-Segregation	Treated Film Pre-Segregation	Treated Film Post-Segregation
τ_1 (ps)	0.346 ± 0.011	0.368 ± 0.011	0.319 ± 0.012	0.348 ± 0.016
τ_2 (ps)	10.09 ± 0.31	7.34 ± 0.23	6.01 ± 0.22	4.40 ± 0.23
τ_3 (ps)	63.0 ± 1.5	51.9 ± 1.14	46.5 ± 1.06	41.0 ± 1.07
τ_4 (ps)	1079 ± 34	896 ± 25	1022 ± 27	902 ± 28

Table 1. Time constants calculated by fitting the data displayed in Figure 11. Fits were performed on averaged TA spectra from all interrogated spots on the untreated film averaged over the first 25 TA scans and averaged over one hour of TA scans after exposure to the migration laser. Time constants from fits performed on average TA spectra from 13 spots on the treated film during 72 scans before and after exposure to the migration laser.

The results of the global fitting analysis for the pre-segregation TA spectrum of the untreated film, Figure 11a, are displayed using solid lines in Figure 11e. Hot carrier cooling is accounted for by a fast exponential with positive amplitude at high energies and negative amplitude at lower energies, indicating that the TA signal decays on the blue side of the spectra at the same rate as it grows on the red side. The other exponentials collectively describe the longer decay processes, including nonlinear effects produced by the high pump pulse intensity necessitated by the low optical density of the NC films. The presence of nonlinear contributions is confirmed by comparison to spectra collected with reduced pump pulse intensity, Figure 14. The longest exponential (red in Figure 11e) likely arises from populations involved in radiative recombination, as the amplitude spectrum of this exponential overlaps well with the PL spectrum of the NCs, Figure 15.

We describe the overall relaxation kinetics using a weighted average of the exponential time constants, excluding the exponential ascribed to hot carrier cooling. Similar to other reports,[100] the weighted average time constant was calculated across the measured wavelength range, weighting by the positive

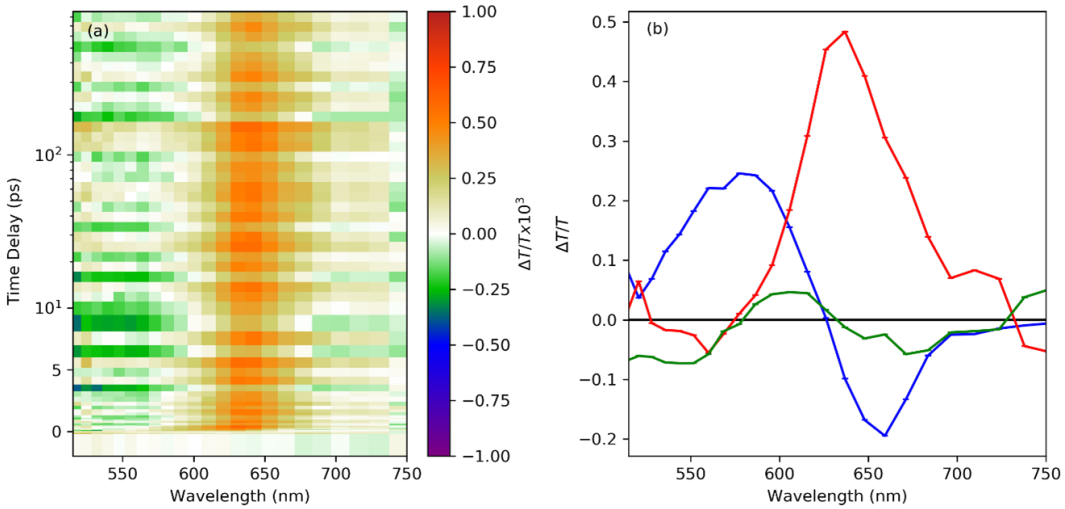

Figure 14. a) TA spectra from one location on the untreated film. b) Global fitting results of the data in (a), fitting to three exponentials. The fit time constants are 2673 ± 733 ps (red), 32.73 ± 14.9 ps (green), and 0.414 ± 0.07 ps (blue). The amplitude of the middle time constant component is much reduced relative to higher-power experiments, indicating that it is mostly due to nonlinear effects induced by the high pump energy. The time constant of the long component is also substantially longer than in experiments with a greater pump intensity, indicating that recombination in the higher-energy experiments was a combination of bimolecular recombination and Auger recombination.

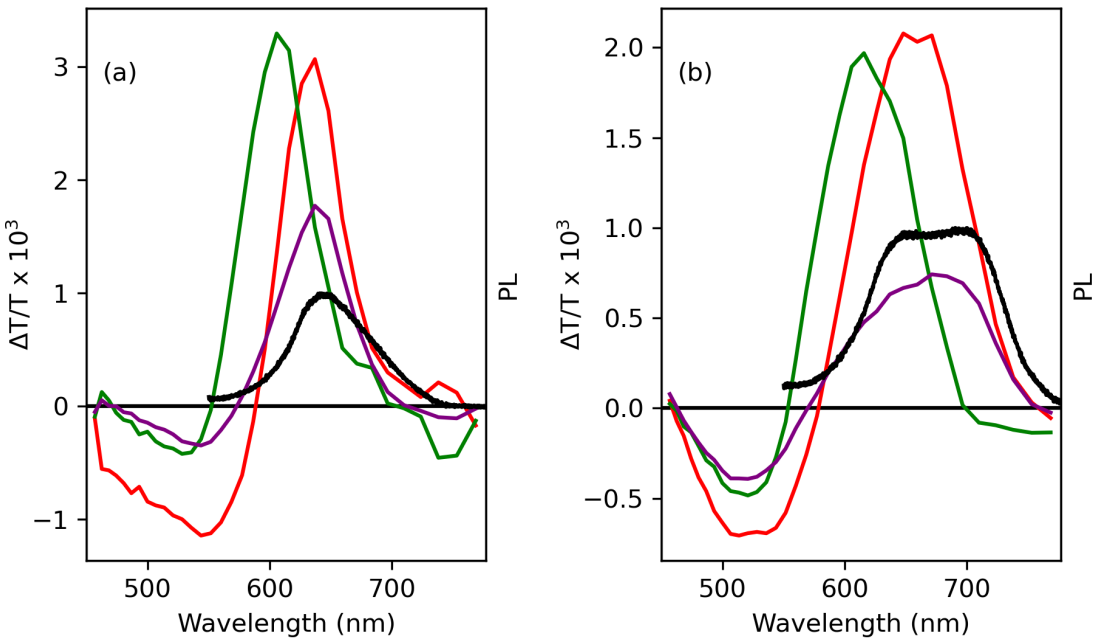

Figure 15. Medium (green), longer (red), and longest (purple) amplitudes from global fits of TA spectra of untreated NCs before (a) and after (b) halide segregation are overlayed with normalized PL spectra (black) collected during exposure of one spot initially (a) and after 30 seconds of illumination (b) with the migration laser. The overlap between the PL spectra and the longest global fit components indicates that the states involved in these decay processes are also involved in emissive recombination.

amplitude at each wavelength for each of the longest three exponentials in the fit:

$$\tau_{weightedaverage} = \sum_{\lambda=457\text{ nm}}^{769\text{ nm}} \frac{\tau_2 A_2(\lambda) + \tau_3 A_3(\lambda) + \tau_4 A_4(\lambda)}{\sum_{\lambda=457\text{ nm}}^{769\text{ nm}} A_2(\lambda) + A_3(\lambda) + A_4(\lambda)} \tag{3.2}$$

The amplitude for each exponential at each wavelength is only included if it is positive, indicating signal originating from ground state bleach or stimulated emission, both of which report on the population of excited NCs. In this equation, the range of wavelengths is between 457 nm and 769 nm and the amplitudes A_2, A_3, and A_4 are those applied to the intermediate time constant, the long time constant, and the offset term, respectively, as in Equation 3.1. By this method, a weighted average time constant of 250 ps was found as an estimate for the untreated film before halide segregation, i.e. for the TA data displayed in Figure 11a.

Next, we compare the TA signal before halide segregation (Figure 11a) to the TA signal after halide segregation has been prompted by one hour of exposure to the TA pump pulse and an additional exposure to the migration laser (Figure 11c). The duration of the exposure to the migration laser was varied between 6 s and 60 s, always enough to cause a notable redshifting in the PL spectrum, even at those spots where halide segregation was not initiated by the TA pump pulse. In Figure 11c, we display the average of the TA signals for one hour after exposure to the 405 nm laser, averaged over all 12 interrogated spots on the sample. The broad bleach feature redshifts considerably after halide segregation, particularly in the spectra for the three long components in the global fits as well as the region of negative amplitude in the short component, shown by the dashed lines in Figure 11e. The redshifting of the negative region in the short component shows that the hot carriers are cooling to states that shift to lower energies as halide segregation

proceeds. The weighted average time constant from this global fit is 186 ps, shorter than the 250 ps calculated before halide segregation.

Exposure to the pump pulse induced halide segregation at nine of the twelve interrogated spots on the sample of untreated NCs. We calculated a 25-scan rolling average of the TA signal over time and find the weighted average time constant for each 25-scan window. The evolution of this quantity over time reveals that the overall relaxation process speeds up as halide segregation is occurring, visible in Figure 11g as a shift to shorter time constants. This shift to faster dynamics with halide segregation is supported by recent observations by Darmawan et al., who showed that recombination dynamics slow down when the halides in $CsPb(Br_xI_{1-x})_3$ NCs become well-mixed.[20]

These symptoms of halide segregation processes are found to be much less influential in the NC film with ligand treatment. The TA signal does not redshift by as much, even after exposure to the migration laser, Figure 11b,d. This is visible in the global fitting analysis, where the amplitude spectra for each of the processes do not redshift to nearly the same degree as observed in the untreated film, Figure 11f. Additionally, the weighted average time constants do not change according to any trend during the initial TA scans, only speeding up after exposure to the migration laser. This indicates that treating the surface of the NC helps prevent the process of halide segregation.

3.3 SSTA Results During NC Synthesis

In recent work led by Dr. James Sadighian in which I helped collect experimental data, we used SSTA spectroscopy to investigate the growth mechanisms of perovskite NCs during the solvation-mediated technique described in section 2.2.2. We noted TA spectral line shapes resembling the derivatives of

the absorbance spectrum.[8] An earlier report of these line shapes in 2D perovskites attributed a first derivative-like component to redshifting of the absorbance spectrum due to the electric field effect generated by spatially separated charge carriers, an effect discussed in section 1.2.[101] The second derivative component was attributed to an overall broadening of the absorbance spectrum, which may arise from the presence of a large number of randomly-oriented dipoles in the sample. The electric field effect could arise in NCs via the trapping of an electron or hole at the NCs surface, indicating poor surface ligation. Thus we investigated the contribution of the first and second derivative features over time during NC synthesis.

To track the contributions of the first derivative-like and second derivative-like line shapes in the TA spectra over time, we fit a spectral slice of TA data to a linear combination of the first and second derivatives of the absorbance spectrum of each NC sample, along with the TA signal of fully-grown NCs. The contributions of these three components to the TA spectral slice over the course of NC synthesis are displayed in Figure 16. We noted significant differences in the observed trends of the first derivative-like and second derivative-like components over time. While the contribution of the first derivative-like component decreases over time, the contribution of the second derivative-like feature is observed growing between 30 and 70 minutes of synthesis time. The disagreement in these trends suggests that the electric field effect may not be sufficient to explain both the first and second derivative-like features.

In this section, I will discuss new SSTA experiments and analysis I have led aimed at elucidating the reason behind the disagreement in these trends. Whereas previous analysis suggests that both the first and second derivative-like

features may arise due to the electric field effect, it is known that the biexciton binding energy, discussed in section 1.2, should also contribute to the TA spectra of NCs throughout their growth. Thus, an experiment that separates the impact of the biexciton binding energy from the electric field effect may enable a better understanding of the TA signals as they evolve. It has been reported that NCs exhibit a stronger size-dependence of the biexciton binding energy when excited near the band gap.[102,103] Therefore we collected TA signals of NCs during growth using a redder pump wavelength. Whereas in our previous report we excited the NCs at 520 nm, in these experiments we excite at 605 nm. During the experiment, we collect absorbance and PL spectra of aliquots withdrawn from the reaction mixture at several times, Figure 17.

TA data from three times during synthesis collecting using a 605 nm pump pulse are displayed in Figure 18. At this redder wavelength, we find that initially the TA signals are rather weak, indicating that nascent NCs during the early stages of the synthesis are not excited at this wavelength. This is also visible in their absorption spectrum, which only begins appreciably absorbing at 605 nm starting at around 20-30 minutes. At around 30 minutes of synthesis time, there

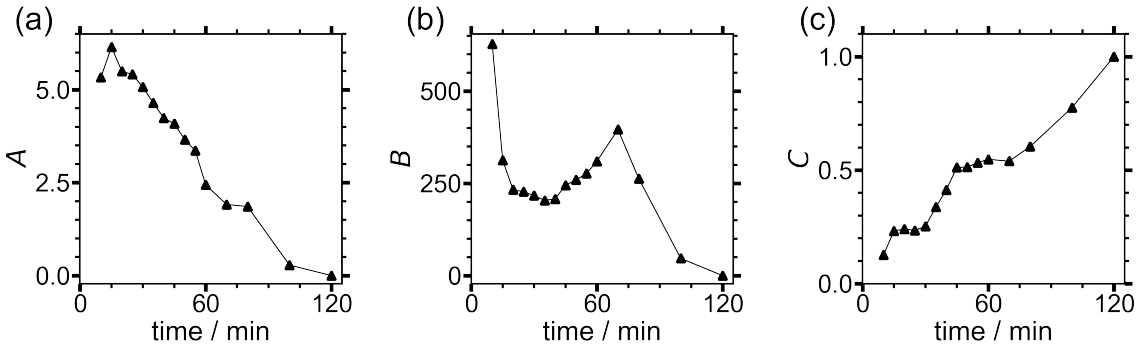

Figure 16. Magnitude of fit coefficients, called A, B, and C, to the first (A) and second (B) derivatives of the absorption spectrum and the TA signal of mature NCs (C). This figure is recreated from reference 8.

is a positive TA signal at 575 nm that grows in at a pump-probe time delay of 30 ps which was not present at earlier synthesis times, or in the TA spectra from our previous report. This signal disappears after more synthesis time, not appearing in the spectrum collected after 60 minutes of stirring. These signals are unlike those seen previously,[8] and thus careful interpretation may yield an enhanced understanding of the evolution of NCs during growth. Here I present a tentative initial interpretation.

That this signal grows in after 30 ps indicates that the states responsible for this signal are not initially populated upon excitation of the sample, but become populated after 30 ps of relaxation time. This signal may arise due to electrons or holes becoming trapped at the NC surface. The appearance and disappearance of this signal as the synthesis proceeds may indicate that there is a period during synthesis during which some population of nascent NCs breaks apart, exposing unpassivated surfaces that enable surface trapping of charge carriers. The fragments of these broken NCs in solution may provide material toward the growth of larger NCs, in a process called Ostwald ripening.[87,104] Future experiments could help elucidate whether this interpretation is appropriate by tracking the wavelength of the positive feature over time. If the positive feature blueshifts over time, it would indicate that the NCs exhibiting this feature become smaller as the reaction proceeds, supporting the interpretation that they are indeed breaking apart.

These initial results will serve as a step toward continued investigation of the evolution of NCs during growth. The separation of contributions of the biexciton binding energy and the electric field effect remains a promising strategy for enabling interpretation of TA line shapes during NC growth. This strategy may offer new insight into the passivation of the NC surfaces over time. Global fitting

analysis of these initial results may offer insight into the relative contributions of the electric field effect and the biexciton binding energy at different pump-probe time delays. Additionally, characterization of the size distribution of NCs during growth, for example via small angle x-ray scattering experiments, may enable estimations of the magnitude of the electric field that could be generated by charge carrier trapping at the NC surface.

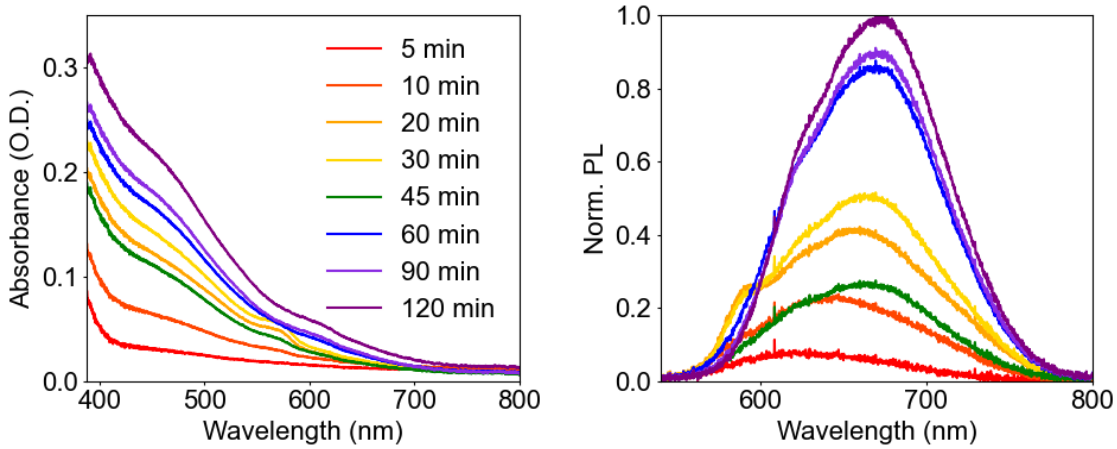

Figure 17. Absorbance and photoluminescence spectra at various times during the synthesis of $MAPbI_3$ NCs. The absorbance at 605 nm is initially small, and grows over time.

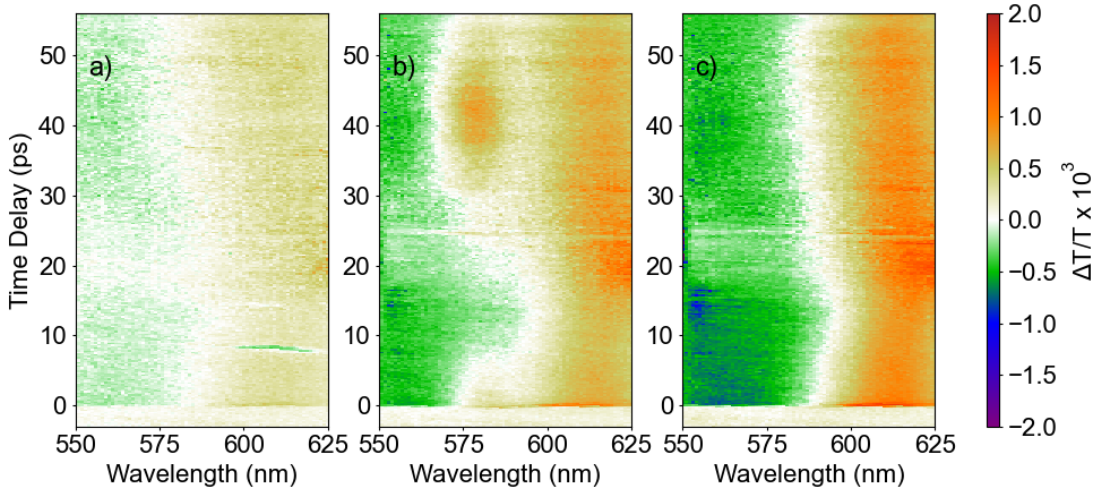

Figure 18. Preliminary SSTA spectra of $MAPbI_3$ NCs after (a) 10 minutes, (b) 30 minutes, and (c) 60 minutes of synthesis time. In the 30 minute spectrum, a positive signal grows in after 30 ps which is not present in the other spectra.

CHAPTER IV

NANOCRYSTAL SIMULATIONS

This chapter includes co-authored material from work in preparation, in which I describe the computational method and results presented in this chapter.

4.1 Effective Mass Approximation

While interpreting our spectroscopic data presented in Chapter III, it was helpful to use computational simulations of model NCs to determine whether our experimental results would support or refute proposed mechanisms. We therefore set out to simulate model NCs during halide segregation using the effective mass approximation, adapting methodology described by Haus et al. and Cheche et al.[105,106] Computational details are described in section 4.1.1.

To rationalize the result that halide segregation is accompanied by both a speeding up of the recombination dynamics and a redshifting of the PL spectrum, we develop a model to emulate the NC during halide segregation. According to the polaron-mediated mechanism proposed by Bischak et al., photoinduced halide segregation proceeds when a photogenerated polaron is stabilized within an iodide-rich region.[73] Over time subsequent polarons become trapped in the iodide-rich region and accumulate more iodide. The iodide-rich region gradually migrates toward the surface of the NC over time. The band structure of the NC depends strongly on the halide content of the lattice, so the development of an iodide-rich region within the NC surrounded by a bromide-rich lattice may be modeled as a heterostructure. Since iodide-rich NCs have band edges within the bandgap of bromide-rich NCs, the migration of one halide to the surface while the other remains deeper within the NC may cause the NC to behave like a type-I or reverse type-I heterostructure. The development of heterostructure-like behavior may

serve to confine the charge carriers to a small part of the NC. It is reported in the literature that Auger lifetimes increase linearly with NCs size.[107] Thus, confinement of the charge carriers to a smaller volume within the NC as halide segregation proceeds may explain the increased rate of Auger recombination observed in our TA results.

In this work, the direction of the PL spectral shift and the charge carrier distributions are estimated using a model spherical NC. We compare the results predicted by two models: a core-shell model, and a many-layers model. In both cases, we choose to model spherical NCs of radius 8 nm, emulating the size of our cubic NCs of side length 16 nm. In the core-shell model, the NC is approximated as a core with a certain halide composition surrounded by a shell with a different halide composition, Figure 19a-c. In the second model, here called the many-layer model, the NC is approximated as an arbitrary number of layers of varying halide compositions, Figure 19d-f. In this work, we use 13 layers for this model, since approximately 13 unit cells would fit within the 8 nm radius of the modeled NC if the perovskite lattice is cubic and has a lattice constant of approximately 6.279 Å as reported in the literature for $MAPbI_3$.[108] The use of multiple layers provides smoother variation of halide composition while maintaining computational accessibility. In each model, the NC and the wave functions of the electron and hole are each assumed to be spherically symmetric, and charge carriers are taken to experience zero potential in the most iodide-rich layer, nonzero potentials in every other layer within the NC, and infinite potential outside the NC.

The halide distribution within the NC is modeled over time, starting from a uniform distribution. The motion of iodides within the NC is modeled iteratively by simulating the net transport of iodides between layers in the NC for a series of

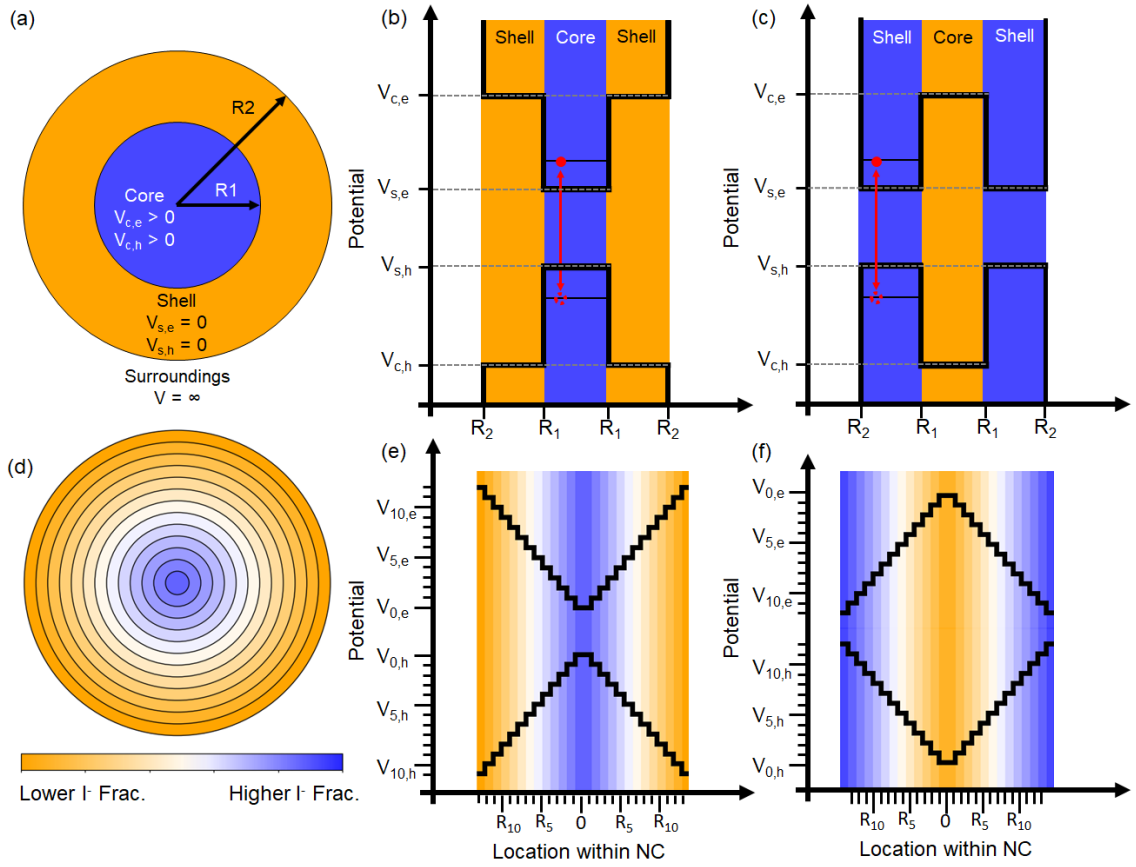

Figure 19. Illustrations of the two NC heterostructure models. a) The core-shell model has only two layers: a core of one halide composition surrounded by a single shell of a different composition. b) Potential within each region of the NC using the core-shell model in the case where iodide anions go to the surface, with 0 set at the potential within the shell, and an infinite potential outside the NC. This band structure emulates that of a reverse type-I heterostructure. c) Potential within each region of the core-shell model in the case where bromide anions go to the surface. This band structure emulates a type-I heterostructure. d) The many-layer model contains layers of varying halide composition, e) Potential within each region of the NC using the many-layer model in the case where iodide anions go to the surface, with 0 set at the potential at the surface. f) Potential within each region of the many-layer model in the case where bromide anions go to the surface, with 0 set at the potential at the center. In all cases, the recombination energy (red arrow) is the sum of the energies of the electron, the hole, and the bandgap in the iodide-rich region. The overall radius of the NCs for the simulations in this work was set to 8 nm. In the many-layer model, each layer is of equal thickness.

time steps. The motion of iodides is modelled as being random in the absence of strain, with the quantity of iodides exchanged between layers being proportional to their shared surface area and the difference in iodide concentration between them. The net migration of iodide toward the center of the NC is driven by strain applied within the model. A large polaron within Map Bx_3 materials has a size on the order of hundreds of unit cells, which is far larger than the size of our NCs. When such a polaron is generated within an NC, there are reports that the dilation of the lattice in response to strain due to the polaron is intense in the middle of the NC and less at the surface.[109] We therefore approximate that the strain is distributed as a Gaussian, with more strain within the center of the NC and less strain at the surface. In the model proposed by Bischak et al., the presence of polaronic strain within a region biases the transport against the migration of iodide away from that region,[73] and so in our model the speed of iodides leaving each layer is inversely proportional to the strain within that layer. During each time step, the total quantity of iodide within each layer is recalculated using the following formula:

$$I(x,t) = I(x,t-1) + T_{In}(x,t) - T_{out}(x,t) \tag{4.1}$$

$$\begin{aligned} T_{In}(x,t) = f\Bigg(&\left[SA(x-1)I_{frac}(x-1,t-1)\frac{1}{S(x-1)}\right] \\ &+ \left[SA(x)I_{frac}(x+1,t-1)\frac{1}{S(x+1)}\right]\Bigg) \end{aligned} \tag{4.2}$$

$$T_{Out}(x,t) = fI_{frac}(x,t-1)\frac{1}{S(x)}\left(SA(x-1) + SA(x)\right) \tag{4.3}$$

where x is a sequential index number assigned to a layer within the NC, t is the time step, $I(x,t)$ is the quantity of iodide within layer x, $I_{frac}(x,t)$ is the iodide fraction within layer x, $T_{In}(x,t)$ is the quantity of iodide transported into layer x from the surrounding layers, $T_{Out}(x,t)$ is the quantity of iodide transported out

of layer x into the surrounding layers, $SA(x)$ is the surface area between layers x and $x + 1$, $S(x)$ is the strain within layer x, and f is a factor that sets the iodide transport rate. Because the strain term is multiplied by an arbitrary factor f, the precise strain values chosen for each layer are arbitrary.

The evolving halide distribution for a Gaussian strain profile using a value of 0.011 for f is compared to the evolving halide distribution for the core/shell model using a value of 0.00016 for f in Figure 20a-c. These values of f were chosen such that the halide distribution reaches a steady state after 10000 time steps. The final halide distribution arises more quickly in the core-shell model as there are only two layers and one interface through which halides can move. In order to compare the two models with similar halide segregation rates, a smaller value of f for the core/shell model was used. For this comparison, the radius of the core in the core/shell model was chosen to be 3 nm, approximating the radius of the region in the many-layers model that becomes enriched. For both models, the strained region in the center of the NC gradually accumulates iodide over time until a region around the core becomes saturated in iodide. Because the layers at the center of the NC are of lesser volume than the layers at the NC surface, the iodide fraction near the center changes much faster than near the surface for a certain quantity of iodide transferred. Both the many-layers model and the core-shell model predict migration of iodide toward the high-strain region in the core and the shift of both the electron and hole towards the new iodide-rich region, Figure 20d-g, but the abrupt interface in the core-shell model is likely sharper than the iodide concentration gradient in actual NCs undergoing halide segregation. The increased number of layers allows a more realistic prediction of the evolving electron and hole wave functions during halide segregation. For example, as is visible in Figure

20e,g, a small amount of iodide continues to move toward the center of the NC between time steps 1000 and 10000 in the many-layer model, expanding the region with diminished bandgap. This decreased potential in the center of the NC allows the electron to delocalize slightly, while simultaneously more effectively confining the hole at the center. We proceed to use the many-layers model to examine the recombination energy and confinement of the electron and hole when strain is applied to the center of the NC.

Using the modelled halide distribution as it evolves over time, the resulting wave functions for the electron and hole are estimated by employing the effective mass approximation, adapting methods reported by Cheche et al. and Haus et al.[105,106] The energy for each charge carrier is determined by finding the energy value that minimizes a cost function constructed from continuity constraints on the wave function. After this energy is found, orthonormalization constants for the wave function of the charge carrier within each layer are found. The wave functions of the electron and hole can then be plotted as a function of radial position within the NC. More information on the computational methods employed here is available in section 4.1.1.

After calculating the wave functions for the electron and hole in the modelled NC, the recombination energy is determined by the following equation:

$$E_r = E_e + E_h + E_g \tag{4.4}$$

Where E_r is the recombination energy, E_e is the energy of the electron over the conduction band minimum in the most iodide-rich region, E_h is the energy of the hole over the valence band maximum in the most iodide-rich region, and E_g is the width of the band gap within the most iodide-rich region of the simulated NC. The

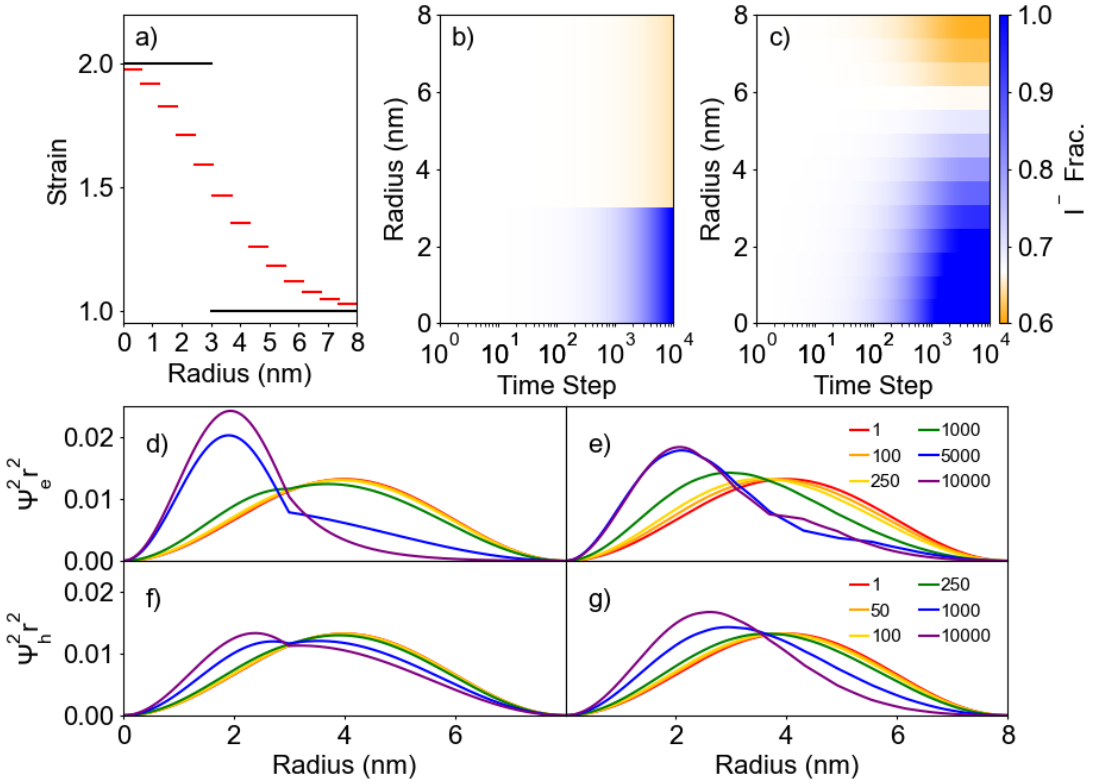

Figure 20. (a) Strain values in the core/shell model (black) and for each of the 13 layers in the multi-layer model (red). The strain in the multi-layer model is distributed according to a Gaussian distribution centered at the radius = 0 within the NC. (b) The iodide fraction as it evolves over 10000 time steps for the core/shell model using factors f = 0.00016 and (c) the many-layer model using factors f = 0.011. Over time the iodide within the NC gradually redistributes from an even distribution to an iodide-rich core surrounded by a relatively iodide-poor shell. The many-layer model prevents the evolution of a sharp interface between the iodide-rich core region and the iodide-poor surface region. The wave functions of the electron (d,e) and hole (f,g) for the core/shell model (d,f), and the many-layer model (e,g) are displayed after a number of iterations shown in the legends. Both models predict that the electron and hole will localize nearer to the core after the halides redistribute in response to the strain in the NC.

value of E_g decreases during halide segregation as the iodide builds up in the layers with the highest strain.

As iodide segregates toward the center of the NC (Figure 21a,c), it is observed that the wave functions of the electron and hole shift toward the NC center (Figure 21b). The energies of the electron and hole, and therefore the recombination energy, shift to lower values, Figure 21e. The rate of Auger recombination should be linearly dependent on the electron-hole overlap and inversely proportional to the volume in which they are overlapped.[110] Thus, we define an overlap-confinement integral by dividing the overlap integral, which depends on r^2, by the volume of their overlap, which depends on r^3. This leaves an overall argument of $\Psi_e\Psi_h/r$ within the integral. The overlap confinement integral increases as halide segregation proceeds, indicating that the charge carriers are confined together within a smaller region in the center of the NC after halide segregation, Figure 21d. At the beginning of the halide segregation process the electron wave function shifts toward the center of the NC more rapidly than the hole, which decreases the overlap integral, Figure 21f. However, the volume term in the integral causes the overlap-confinement integral to substantially increase during this period of halide segregation, Figure 21d. Thus, the rate of Auger recombination should increase during halide segregation. Electron delocalization during later time steps is visible as a small decrease in the overlap-confinement integral, which could result in a small decrease in Auger recombination rate, though this was not observed in our measurements. Overall, the substantial increase in the overlap-confinement integral after halide segregation relative to the initial state would cause a faster rate of Auger recombination after halide segregation,

in agreement with our spectroscopic results. Meanwhile, the recombination energy decreases, in agreement with the observed photoluminescence redshifting.

It is commonly stated in the literature that iodide anions segregate toward the surface of the perovskite, in disagreement with the present model in which iodide segregates toward the core.[82,85,111,112] Here we explore two possible ways in which our model could produce an iodide-rich region at the surface: halide segregation directly toward the surface of the NC, and the gradual migration of the iodide-rich core toward the NC surface as a unit.

We first consider individual iodide anions preferentially migrating toward the surface of the NC, leaving behind a bromide-rich core, Figure 22a, by setting the strain at the surface of the NC to be higher than the core, Figure 22b. During segregation the electron localizes into the outermost few layers faster and more completely than the hole, Figure 22b. While this separation does not substantially diminish the overlap of the electron and hole, Figure 22f, the confinement-overlap integral is lower throughout segregation compared to its initial state, Figure 22d. This indicates that the Auger recombination rate should decrease, contradicting our TA measurements. Even when both carriers have shifted toward the surface, the recombination energy is predicted to blueshift owing to the remaining wave function density in the iodide-depleted regions near the center of the NC, Figure 22e. These results suggest that the iodide anions do not segregate directly toward the surface, but rather migrate toward the surface after the iodide-rich region has developed.

Instead of biasing individual iodide anions to move towards the surface, we next investigate the case where an iodide-rich core migrates toward the surface as a unit. This is similar to the mechanism proposed by Bischak et al. in which

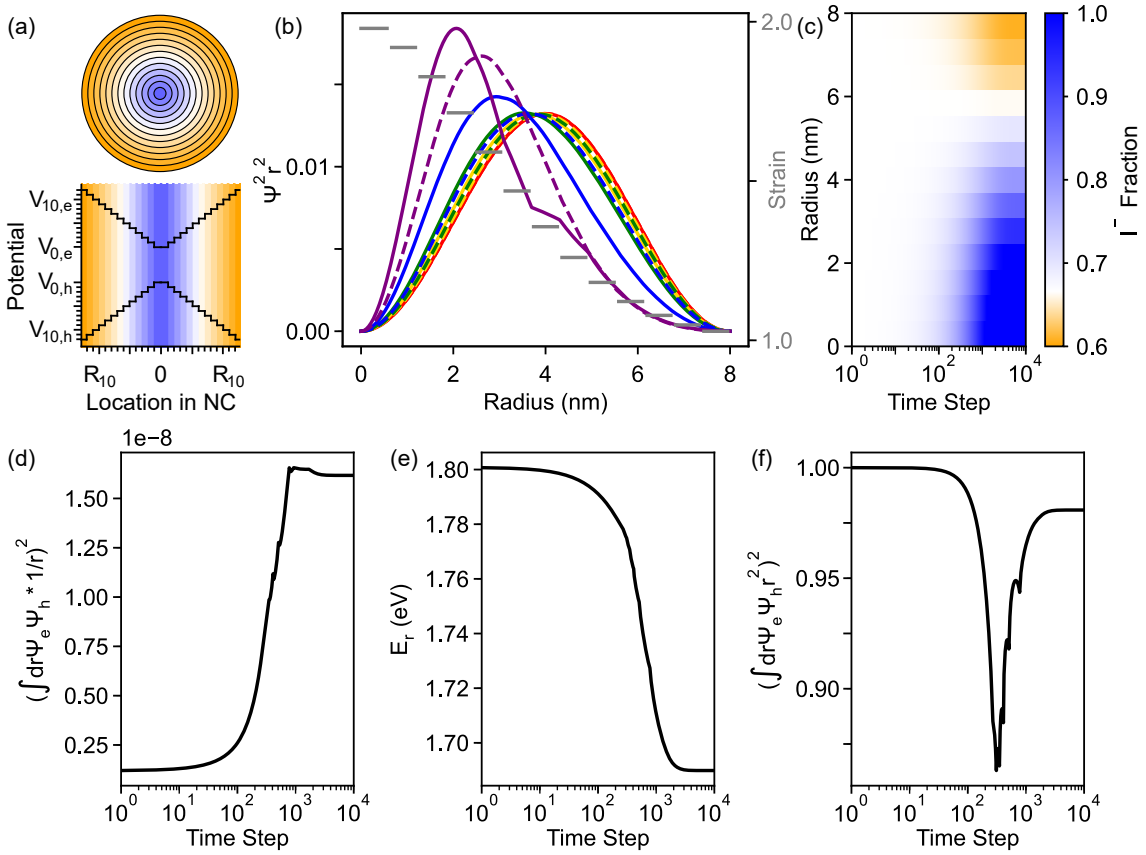

Figure 21. (a) Schematic showing many-layer model (top) and the potential for the electron and hole in each layer (bottom). Colors indicate the type of type-I heterostructure that would form in a polaronic strain model, blue indicates a larger iodide fraction than orange. (b) As iodide migrates toward the NC center due to strain (gray), the electron (solid) and hole (dashed) wave functions shift inward. Wave functions after 1 (red), 50 (yellow), 100 (green), 250 (blue), and 10000 (purple) time steps. (c) Evolving iodide fraction over 10000 time steps. From an even distribution, iodide gradually migrates to form an iodide-rich core surrounded by a relatively iodide-poor shell. (d) Overlap-confinement integral increases as halide segregation proceeds, indicating that they become more overlapped within a smaller area over time. (e) Recombination energy decreases over time, in agreement with spectroscopic evidence. (f) Electron-hole overlap is strong after an initial decrease as the electron shifts toward the center faster than the hole.

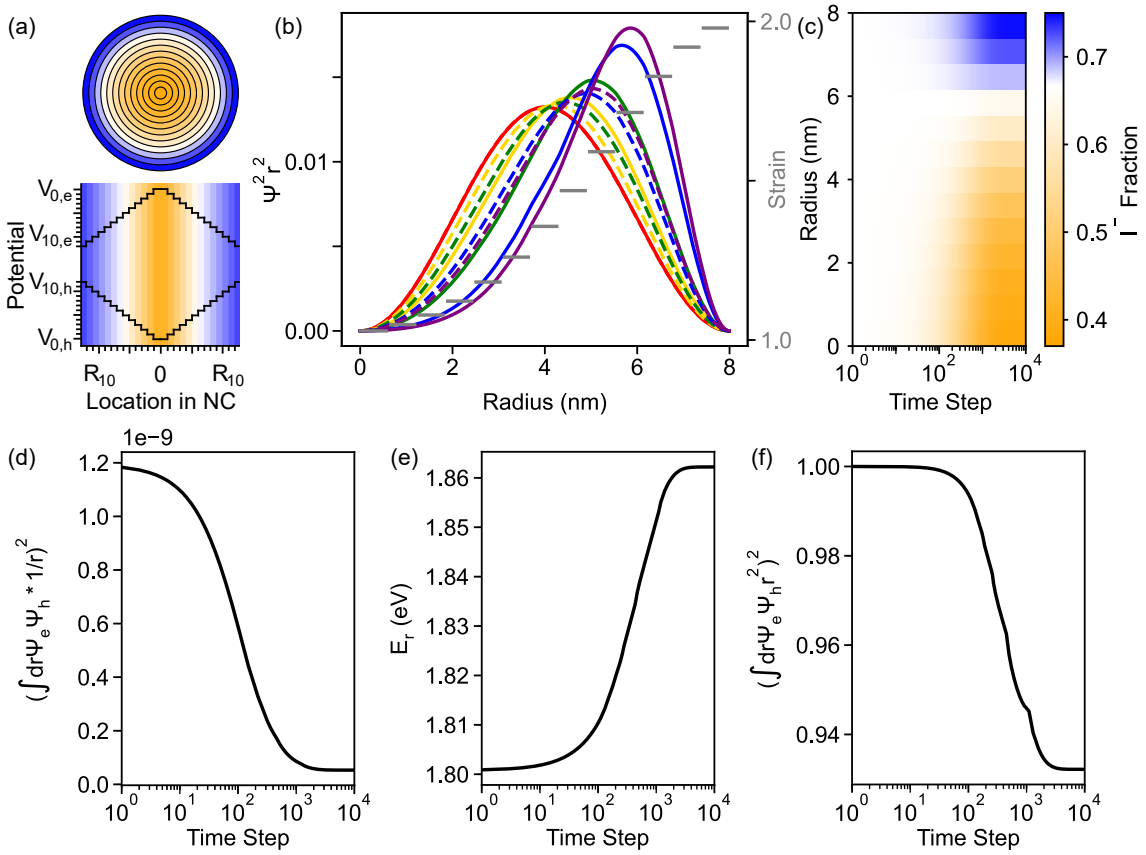

Figure 22. (a) Schematic showing many-layer model (top) and the potential for the electron and hole in each layer (bottom). Colors indicate the reverse type-I heterostructure that would form if iodides segregated to the NC shell, blue indicates a larger iodide fraction than orange. (b) As iodide migrates toward the NC surface due to strain (gray), the electron (solid) and hole (dashed) wave functions shift toward the surface. Wave functions after 1 (red), 100 (yellow), 250 (green), 1000 (blue), and 10000 (purple) time steps. (c) Evolving iodide fraction over 10000 time steps. From an even distribution, iodide gradually migrates to form an iodide-rich shell surrounding a relatively iodide-poor core. (d) Overlap-confinement integral decreases as halide segregation proceeds due to diminished overlap and the shift of both charge carriers away from the NC center. (e) Recombination energy increases over time, contradicting spectroscopic evidence. (f) Electron-hole overlap diminishes as the electron shifts toward the surface faster and more completely than the hole.

iodide-rich regions form within the NC due to polaronic strain. These regions may then tend to migrate toward the surface over time during illumination.[73] As we are assuming that the iodide-rich region forms in the core of the NC prior to its migration to the surface, we use the simpler core-shell model to model the iodide-rich region, as the final result of iodide segregation is similar for the two models, Figure 20d-g. We model an NC composed of an iodide-rich region (blue in Figure 23a) of radius 3 nm (yellow line), surrounded by iodide-poor material (orange in Figure 23a) for a total NC radius of 8 nm (combined lengths of the yellow and solid black lines). The inner region is assigned an iodide fraction of 1 and the surroundings are assigned an iodide fraction of 0.648. These sizes and iodide fractions were chosen to approximate the final state after thousands of time steps using the many-layers model above. The computational method in this work assumes spherically symmetric NCs, but the system ceases to be spherically symmetric when the iodide-rich core migrates away from the center of the NC. We calculate estimated wave functions by considering a line segment with one end at the center of the iodide-rich region and the other on the surface of the NC. The distances along this line segment which fall within each region (indicated in Figure 23a) are used as the radii for a core/shell NC simulation, from which the recombination energy and particle wave functions are extracted. The line segment is then rotated about the center of the iodide-rich region by small angular steps and the simulation is repeated for each new set of distances. Once the line segment has been rotated in a complete circle, the average value of the recombination energy is determined using the following equation:

$$Avg.E_r = \frac{1}{2\pi}\int_0^{2\pi} E_r(\theta)d\theta \tag{4.5}$$

Once the simulations are recorded and the average recombination energy is determined, the iodide-rich region is moved by a small distance toward the NC surface (along the dotted black arrow in Figure 23a) and the process is repeated. By this method we determine the wave functions of the electron and hole during the migration of the iodide-rich region to the surface and obtain an approximation of the recombination energy during the migration process.

The electron and hole stay confined to the iodide-rich region throughout its migration toward the surface, Figure 23b. Even when interrogating angles for which the size of the surroundings dwarfs the size of the iodide-rich region, the electron and hole maintain confinement within the iodide-rich core. Lower particle energies are calculated along angles where there is more material between the center of the iodide-rich region and the surface of the NC, and greater energies along angles where there is less, Figure 23c. The average of the recombination energy as the iodide-rich region migrates from the center to the surface lies between 1.72 eV when the iodide-rich region is at the center of the NC, to 1.77 eV when it is at the NC surface, in contradiction to experimental results, Figure 23d. However, the final recombination energy is still redshifted from the recombination energy prior to halide segregation (1.77 eV after migration to the surface vs 1.80 eV prior to segregation), and it is possible that the two stages of migration we have outlined (i.e. strain-driven formation of iodide-rich regions within the NC and their migration to the NC surface) occur in concert. Additionally, a model that more rigorously accounts for the breakdown of spherical symmetry during the migration of the iodide-rich core to the surface is likely to yield lower recombination energies. The current model assumes that the wave function will be centered at the center of the iodide-rich region, but as this region approaches the infinite potential at

the surface of the NC, the center of the wave function is likely to shift towards the center of the NC, decreasing the confinement and redshifting the energy. However, the observed result that the electron and hole each stay confined to the iodide-rich region supports that this mechanism, wherein and iodide-rich region forms within the NC and migrates to the surface, is in closer agreement with our spectroscopic evidence than a model where the iodide anions would segregate directly toward the surface.

Taken together, these simulations suggest that our transient absorption results support a mechanism where iodide-rich regions form within the NC and migrate toward the surface, rather than the entire surface evenly becoming iodide-enriched over time. The maintenance of confinement of the electron and hole as the I-rich region migrates toward the surface indicates that our reported results are likely explainable using such a mechanism.

In this work, we report observations via globally fitting TA measurements of $MAPbI_xBr_{3-x}$ NC films indicating that halide segregation is accompanied by the speeding up of nonlinear recombination dynamics including Auger recombination. This suggests that after halide segregation, photogenerated electrons and holes have enhanced wave function density within a smaller portion of the NC. We explain these results using a novel computational technique in which the NCs are modelled as a spherically symmetric potential wells, with the potential within each layer varying over time according to its evolving iodide content. Using this computational technique, we establish that our spectroscopic results are best supported by a segregation mechanism in which an iodide-rich region initially forms within the NC and migrates to the surface over time, such as the mechanism proposed by Bischak et al.[73] The reported results allow for the discernment

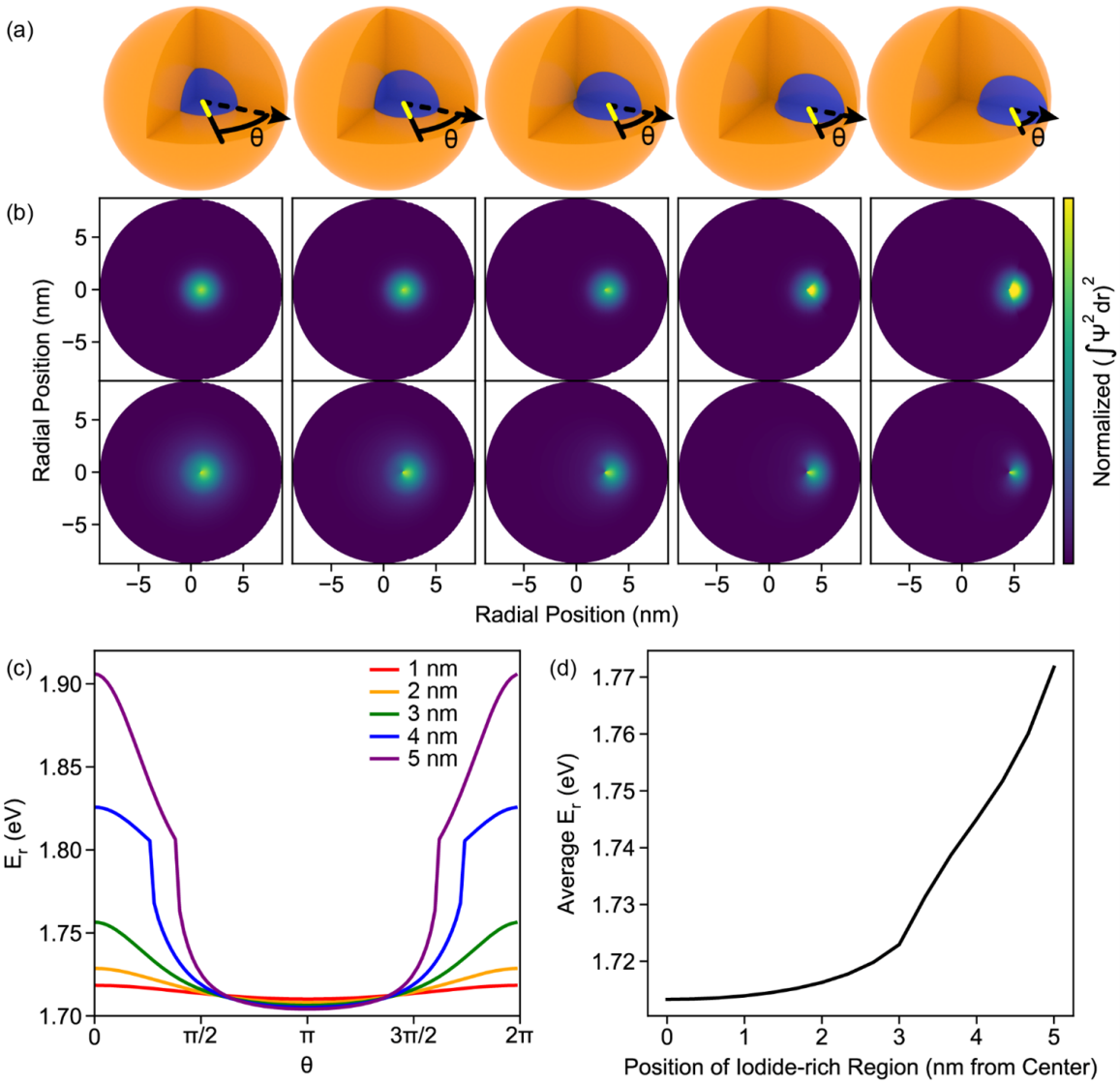

Figure 23. (a) Simulations are performed as the position of the iodide-rich region (100% iodide, blue) shifts from the NC center to the surface (dashed arrow) while surrounded by iodide-poor material (64.8% iodide, orange). The thickness of material in core (yellow) and shell (black) for each value of θ is used for a core-shell simulation. (b) The normalized wave function density of the electron (top) and hole (bottom) show that the carriers are localized within the iodide-enriched region as it migrates toward the surface. Wave function density is normalized along each angle. (c) Recombination energy varies with angle, especially as the iodide-rich region nears the surface. Legend indicates offset of iodide-rich region from NC center. (d) Average recombination energy gradually increases as iodide-rich region migrates to surface.

between this supported mechanism and other possible mechanisms where the iodide anions would directly migrate to the surface. The novel computational technique represents a new tool for the study of halide segregation in mixed-halide perovskite NCs and may prove invaluable for interpreting future spectroscopic characterization.

4.1.1 Mathematical Treatment of Simulation Method. The methodology described here is adapted from sources in the literature.[105,106] Consider a core-shell heterostructure nanocrystal of overall radius 8 nm of many layers with materials such that the potential felt by a particle within any layer is some positive number V above the potential in the most iodide-rich layer material, R_i, where we consider the potential to be zero. Let there be infinite potential outside the nanocrystal.

$$V(r) = \begin{cases} 0 & r \in R_i \\ V(r) & r \notin R_i \\ \infty & r > 8nm \end{cases} \tag{4.6}$$

In each region, the location of the valence band maximum and the conduction band minimum as well as the band gap (E_g) are estimated using a linear equation, based upon data compiled by Noh et al.[58]:

$$\begin{aligned} CBM &= 0.57(1-x) - 3.93 \\ VBM &= 0.14(1-x) - 5.44 \\ E_g &= 0.17(1-x) + 1.51 \end{aligned} \tag{4.7}$$

where x is the fraction of halides in the region which are iodides (from now on called the "iodide fraction"). The radial Schrodinger Equation for this particle is

then:

$$\frac{-\hbar^2}{2m^*(r)}\frac{1}{r}\frac{d^2}{dr^2}[rR_l(r)] + \frac{l(l+1)\hbar^2}{2m^*(r)r^2}R_l(r) = [E - V(r)]R_l(r) \tag{4.8}$$

where r is the radial coordinate, $R_l(r)$ is the radial component of the particle wave function, $\hbar$ is the reduced Planck constant, $m^*(r)$ is the position-dependent effective mass of the particle, l is the angular momentum quantum number, and E is the energy of the particle.

Cheche et al.[105] show that using the change of variable $\rho = k_i r$, where $k_i^2 = \mp 2m_i(E - V_i)$ and i is an integer index for the layer within the NC, the Schrodinger equation can be reduced to the following differential equation:

$$\rho^2\frac{d^2\nu_l(\rho)}{d\rho^2} + 2\rho\frac{d\nu_l(\rho)}{d\rho} - l(l+1)\nu_l(\rho) \mp \rho^2\nu_l(\rho) = 0 \tag{4.9}$$

This differential equation is Bessel's equation of order, which takes the form:

$$x^2\frac{d^2y}{dx^2} + x\frac{dy}{dx} + x^2y - \nu^2y = 0 \tag{4.10}$$

In our case, the x in this form is replaced by ρ, the y is replaced by $\nu_l(\rho)$, and $\nu^2 = l(l+1)$. The solutions to the Schrodinger equation are therefore linear combinations of spherical Bessel functions of the first and second kind (j and y, respectively) and modified spherical Bessel functions of the first and second kind (i and k, respectively) in any region:

$$R(r) = \begin{cases} Aj(k(r)r) + By(k(r)r) & E > V(r) \\ Ai(k(r)r) + Bk(k(r)r) & E < V(r) \end{cases} \tag{4.11}$$

where $k = \sqrt{2m^*(r)|E - V(r)|}/\hbar^2$.

We subject the solutions of equation 4.11 to the following constraints at the boundary between layers n and $n+1$ at radius r_n:

$$\begin{aligned} R_n(r_n) &= R_{n+1}(r_n) \\ \frac{1}{m_n^*}R_n'(r_n) &= \frac{1}{m_{n+1}^*}R_{n+1}'(r_n) \end{aligned} \tag{4.12}$$

These constraints, combined with the constraint that the wave function must equal zero at the surface of the NC and it must be regular at $r = 0$ (i.e. the orthonormalization constant B must be zero within the innermost layer), allow for the isolation of a finite number of valid particle energies. The constraint equations may be organized into a matrix format. An example for n=2 layers, with an internal boundary at $r = r_1$ and the NC surface at $r = r_2$ is shown below:

$$\begin{bmatrix} i(k(r_1)) & -j(k(r_1)) & -y(k(r_1)) \\ \frac{1}{m_1^*}i'(k(r_1)) & -\frac{1}{m_1^*}j'(k(r_1)) & -\frac{1}{m_1^*}y'(k(r_1)) \\ 0 & jk(r_2) & y(k(r_2)) \end{bmatrix} \begin{bmatrix} A_1 \\ A_2 \\ B_2 \end{bmatrix} = \begin{bmatrix} 0 \\ 0 \\ 0 \end{bmatrix} \tag{4.13}$$

This matrix equation has nontrivial solutions only when the determinant of the constraints matrix is equal to zero, in which case it has infinitely many solutions. In order to find the lowest valid particle energy, the determinant of the constraints matrix is used as an error function for fitting via the least squares method. In practice, the determinant of the constraints matrix was calculated using the numpy.linalg package in Python, while the energy fitting was performed using the lmfit package.[113] The recombination energy of simulated NC is found by summing energies of the electron and hole (determined independently) along with the band gap in the most iodide-rich layer in the NC.

Once the energy of the particle is determined via fitting, the orthonormalization constants A and B are determined for each layer in the NC. Starting with the outermost layer, the value of A is first assumed to be some

number A_i, whereupon the value of B can be determined by ensuring that the wave function equals zero at the surface of the NC. Then, using the constraints in Equation 4.12 for each successive layer, the values of A and B are determined for each layer of the NC. This method guarantees that the wave function respects the constraints in Equation 4.12, but does not guarantee that the wave function is normalized. To normalize the wave function, the following cost function is used for fitting A_i:

$$Cost(A_i) = 1 - \int_{r=0}^{r=8nm} r^2 R(r)^2 dr \tag{4.14}$$

With the wave functions of both the electron and the hole normalized, the particle overlap within the NC can be calculated via the following equation:

$$Overlap = \left(\int_{r=0}^{r=8nm} r^2 R_{electron}(r) R_{hole}(r) dr \right)^2 \tag{4.15}$$

CHAPTER V

CONCLUSION

5.1 Future Directions

5.1.1 Leveraging SSTA spectroscopy to more closely observe halide segregation.

I presented in Chapter III TA spectra from $MAPbI_2Br$ NCs before and after halide segregation. The small size and inhomogeneity of the sample films that my collaborators were able to provide precluded the use of the SSTA spectrometer setup, which requires a sample that is homogeneous over a distance of about 22 mm, as discussed in section 2.1.2. For this reason, I instead opted to collect TA spectra from these samples using a traditional TA setup, which can only offer a much slower rate of data collection. To observe the process of halide segregation in finer detail over time, it will be required to develop a method of creating large homogeneous $MAPbI_2Br$ NC films. This will require the development and characterization of a repeatable synthetic technique accessible to our lab that yields $MAPbI_2Br$ NCs, as well as a method of reliably casting and encapsulating homogeneous NC films. Once samples that are compatible with SSTA can be easily fabricated, the faster data collection speed accessible via SSTA can be leveraged to gain more detailed insight into the process of halide segregation in these NCs. Once this has been achieved, further investigations into the mechanism and prevention of halide segregation can be pursued. For example, our collaborators found benefits to using a mixture of EDTA and L-glutathione rather than one or the other.[38] During future experiments, the role of each ligand in the mixture could be elucidated. The impact of different mixtures of surface ligands on the halide segregation process could also be compared.

5.1.2 Determining the mechanism of mixed-halide NC growth.

Over the past several years, our group has investigated the characteristics of NCs during their growth via a solvation-mediated synthesis method. We have largely focused on $MAPbI_3$ NCs during these investigations, and have made strides toward understanding of the development of NCs over time.[8,75] However, we have not yet performed an organized investigation into the growth mechanism of mixed-halide NCs synthesized by the same method. It is unclear whether NCs synthesized with a mixture of halides form and grow with a constant halide composition over time. The freedom of halides to migrate around the lattice allows for the possibility that upon nucleation the NCs contain, in the extreme case, only one halide, with the other inculcating over time according to previously reported syntheses.[25] Insights into the halide composition of NCs during growth will be invaluable to any future attempts to adjust reaction conditions during synthesis to form NCs with targeted properties.

5.1.3 Measuring NC size distribution during growth. Much of the interpretation of the NC growth mechanism we have reported relies on absorbance, PL, and TA spectroscopies to infer the growth of NCs over time. While these techniques do carry size-dependent information, it is not easy to obtain a direct measure of the size distribution of NCs during growth exclusively via these techniques. The development of a method that provides a direct measure of the size distribution of NCs would offer valuable insight into their growth. A technique that is well-suited to the measurement of samples during solvation-mediated syntheses would need to accept samples in the liquid state and perform its analysis relatively quickly, before the NC population evolves appreciably. To this aim, small angle x-ray scattering may be employed, as it can expediently offer size distribution

information of NCs in solution. The measurement of fully-grown NCs by a direct-detection TEM method may additionally yield valuable information on the size of NCs after synthesis.

5.2 Conclusions

In this dissertation, I present investigations into the mechanism of halide segregation in perovskite NCs. I present in Chapter I an introduction to the problem of halide segregation in perovskite NCs. The spontaneous segregation of the halides within perovskite NCs causes narrowing of the band gap, preventing their widespread adoption in light emitting or absorbing devices. It is reported in multiple studies that during halide segregation in $MAPbI_xBr_{3-x}$ systems, iodide anions tend to migrate toward grain boundaries and crystal surfaces. This has profound importance for NC systems, for which the surface area to volume ratio is extremely large. The movement of iodides to crystal surfaces suggests that chemical treatment of the NC surface may serve to prevent halide segregation.

A mixture of EDTA and L-glutathione ligands has been found to largely prevent the occurrence of halide segregation.[38] Using the methods presented in Chapter II, I collect and fit TA spectra of NCs that have been treated with this mixture of ligands, and NCs that have not. I present in Chapter III the results of these spectroscopic investigations. Redshifting of the PL and TA spectra is observed to a much larger degree in untreated NCs than in treated NCs, and the relaxation dynamics is observed speeding up after halide segregation. I also report initial spectral results aimed at aiding the interpretation of our previous studies into the mechanism of $MAPbI_3$ NC growth via a solvation-mediated synthetic technique. By using a pump wavelength closer to the band gap of these NCs than our previous experiments, I seek to isolate the contribution of the biexciton

binding energy to the TA spectra from that of the quantum-confined electric field effect. My initial results showing the temporary formation of a positive $\Delta T/T$ signal growing in at a pump-probe time delay of 30 ps may provide insight into the growth mechanism of these NCs with further data collection and analysis.

Using my spectral results from NCs during halide segregation, in Chapter IV I present a computational model to estimate the behavior of iodide anions during the process of halide segregation. Using these calculations, I find that the observed spectroscopic results are better described by the motion of iodide toward the center of the NC, rather than toward the NC surface. The gap between this result and reports in the literature that iodide segregates toward crystal surfaces may be closed by the possibility of iodide-rich regions migrating toward the NC surface as a unit over time. The insights gained through these spectroscopic and computational experiments provide valuable insight into the process of halide segregation in perovskite NCs. Solving the problem of halide segregation will be instrumental to enabling the future widespread adoption of perovskite NCs in practical applications.

REFERENCES CITED

(1) Adinolfi, V.; Ning, Z.; Xu, J.; Masala, S.; Zhitomirsky, D.; Thon, S. M.; Sargent, E. H. Electric field engineering using quantum-size-effect-tuned heterojunctions. *Applied Physics Letters* **2013**, *103*, 011106.

(2) Petryayeva, E.; Algar, W. R.; Medintz, I. L. Quantum Dots in Bioanalysis: A Review of Applications across Various Platforms for Fluorescence Spectroscopy and Imaging. *Applied Spectroscopy* **2013**, *67*, 215–252.

(3) Song, K.; Liu, L.; Zhang, D.; Hautzinger, M. P.; Jin, S.; Han, Y. Atomic-Resolution Imaging of Halide Perovskites Using Electron Microscopy. *Advanced Energy Materials* **2020**, *10*, 1904006.

(4) Wu, X.; Ke, X.; Sui, M. Recent progress on advanced transmission electron microscopy characterization for halide perovskite semiconductors. *Journal of Semiconductors* **2022**, *43*, 041106.

(5) Zhang, D.; Zhu, Y.; Liu, L.; Ying, X.; Hsiung, C.-E.; Sougrat, R.; Li, K.; Han, Y. Atomic-resolution transmission electron microscopy of electron beam–sensitive crystalline materials. *Science* **2018**, *359*, 675–679.

(6) Boles, M. A.; Ling, D.; Hyeon, T.; Talapin, D. V. The surface science of nanocrystals. *Nature Materials* **2016**, *15*, 141–153.

(7) Panthani, M. G.; Hessel, C. M.; Reid, D.; Casillas, G.; José-Yacamán, M.; Korgel, B. A. Graphene-Supported High-Resolution TEM and STEM Imaging of Silicon Nanocrystals and their Capping Ligands. *The Journal of Physical Chemistry C 116*, 22463–22468.

(8) Sadighian, J. C.; Wilson, K. S.; Crawford, M. L.; Wong, C. Y. Evolving Stark Effect During Growth of Perovskite Nanocrystals Measured Using Transient Absorption. *Frontiers in Chemistry* **2020**, *8*, 585853.

(9) Colvin, V. L.; Alivisatos, A. P. CdSe nanocrystals with a dipole moment in the first excited state. *The Journal of Chemical Physics* **1992**, *97*, 730–733.

(10) Walters, G.; Wei, M.; Voznyy, O.; Quintero-Bermudez, R.; Kiani, A.; Smilgies, D.-M.; Munir, R.; Amassian, A.; Hoogland, S.; Sargent, E. The quantum-confined Stark effect in layered hybrid perovskites mediated by orientational polarizability of confined dipoles. *Nature Communications* **2018**, *9*, 4214.

(11) Gao, W.; Ding, J.; Bai, Z.; Qi, Y.; Wang, Y.; Lv, Z. Multiple excitons dynamics of lead halide perovskite. *Nanophotonics* **2021**, *10*, 3945–3955.

(12) Kang, K. I.; Kepner, A. D.; Gaponenko, S. V.; Koch, S. W.; Hu, Y. Z.; Peyghambarian, N. Confinement-enhanced biexciton binding energy in semiconductor quantum dots. *Physical Review B* **1993**, *48*, 15449–15452.

(13) Klimov, V. I. Optical Nonlinearities and Ultrafast Carrier Dynamics in Semiconductor Nanocrystals. *The Journal of Physical Chemistry B* **2000**, *104*, 6112–6123.

(14) Klimov, V.; Hunsche, S.; Kurz, H. Biexciton effects in femtosecond nonlinear transmission of semiconductor quantum dots. *Physical Review B* **1994**, *50*, 8110–8113.

(15) Hu, Y. Z.; Koch, S. W.; Lindberg, M.; Peyghambarian, N.; Pollock, E. L.; Abraham, F. F. Biexcitons in semiconductor quantum dots. *Physical Review Letters* **1990**, *64*, 1805–1807.

(16) Makarov, N. S.; Guo, S.; Isaienko, O.; Liu, W.; Robel, I.; Klimov, V. I. Spectral and Dynamical Properties of Single Excitons, Biexcitons, and Trions in Cesium–Lead-Halide Perovskite Quantum Dots. *Nano Letters* **2016**, *16*, 2349–2362.

(17) Castañeda, J. A.; Nagamine, G.; Yassitepe, E.; Bonato, L. G.; Voznyy, O.; Hoogland, S.; Nogueira, A. F.; Sargent, E. H.; Cruz, C. H. B.; Padilha, L. A. Efficient Biexciton Interaction in Perovskite Quantum Dots Under Weak and Strong Confinement. *ACS Nano* **2016**, *10*, 8603–8609.

(18) Aneesh, J.; Swarnkar, A.; Kumar Ravi, V.; Sharma, R.; Nag, A.; Adarsh, K. V. Ultrafast Exciton Dynamics in Colloidal CsPbBr3 Perovskite Nanocrystals: Biexciton Effect and Auger Recombination. *The Journal of Physical Chemistry C* **2017**, *121*, 4734–4739.

(19) Yumoto, G.; Tahara, H.; Kawawaki, T.; Saruyama, M.; Sato, R.; Teranishi, T.; Kanemitsu, Y. Hot Biexciton Effect on Optical Gain in CsPbI3 Perovskite Nanocrystals. *The Journal of Physical Chemistry Letters* **2018**, *9*, 2222–2228.

(20) Darmawan, Y. A.; Yamauchi, M.; Masuo, S. In Situ Observation of Emission Sites during the Halide Exchange Reaction in Single Cesium Lead Halide Perovskite Nanocrystals. *The Journal of Physical Chemistry C* **2022**, *126*, 2627–2633.

(21) Yoshimura, H.; Yamauchi, M.; Masuo, S. In Situ Observation of Emission Behavior during Anion-Exchange Reaction of a Cesium Lead Halide Perovskite Nanocrystal at the Single-Nanocrystal Level. *The Journal of Physical Chemistry Letters* **2020**, *11*, 530–535.

(22) Wenk, H.-R.; Bulakh, A. G. *Minerals: their contitution and origin*; Cambridge University Press, pp 406–424.

(23) Hirose, K.; Sinmyo, R.; Hernlund, J. Perovskite in Earth's deep interior. *Science 358*, 734–738.

(24) Kojima, A.; Teshima, K.; Shirai, Y.; Miyasaka, T. Organometal Halide Perovskites as Visible-Light Sensitizers for Photovoltaic Cells. *Journal of the American Chemical Society* **2009**, *131*, 6050–6051.

(25) Jang, D. M.; Park, K.; Kim, D. H.; Park, J.; Shojaei, F.; Kang, H. S.; Ahn, J.-P.; Lee, J. W.; Song, J. K. Reversible Halide Exchange Reaction of Organometal Trihalide Perovskite Colloidal Nanocrystals for Full-Range Band Gap Tuning. *Nano Letters* **2015**, *15*, 5191–5199.

(26) Frost, J. M.; Butler, K. T.; Brivio, F.; Hendon, C. H.; van Schilfgaarde, M.; Walsh, A. Atomistic Origins of High-Performance in Hybrid Halide Perovskite Solar Cells. *Nano Letters* **2014**, *14*, 2584–2590.

(27) Walsh, A. Principles of Chemical Bonding and Band Gap Engineering in Hybrid Organic–Inorganic Halide Perovskites. *The Journal of Physical Chemistry C* **2015**, *119*, 5755–5760.

(28) Jin, H.; Debroye, E.; Keshavarz, M.; Scheblykin, I. G.; Roeffaers, M. B. J.; Hofkens, J.; Steele, J. A. It's a trap! On the nature of localised states and charge trapping in lead halide perovskites. *Materials Horizons* **2019**,

(29) Brandt, R. E.; Stevanović, V.; Ginley, D. S.; Buonassisi, T. Identifying defect-tolerant semiconductors with high minority-carrier lifetimes: beyond hybrid lead halide perovskites. *MRS Communications* **2015**, *5*, 265–275.

(30) Walsh, A.; Zunger, A. Instilling defect tolerance in new compounds. *Nature Materials* **2017**, *16*, 964–967.

(31) Du, M. H. Efficient carrier transport in halide perovskites: theoretical perspectives. *Journal of Materials Chemistry A* **2014**, *2*, 9091–9098.

(32) Xue, H.; Brocks, G.; Tao, S. Intrinsic defects in primary halide perovskites: A first-principles study of the thermodynamic trends. *Physical Review Materials* **2022**, *6*, 055402.

(33) Zhao, Q.; Hazarika, A.; Chen, X.; Harvey, S. P.; Larson, B. W.; Teeter, G. R.; Liu, J.; Song, T.; Xiao, C.; Shaw, L.; Zhang, M.; Li, G.; Beard, M. C.; Luther, J. M. High efficiency perovskite quantum dot solar cells with charge separating heterostructure. *Nature Communications* **2019**, *10*, 2842.

(34) Deng, W.; Xu, X.; Zhang, X.; Zhang, Y.; Jin, X.; Wang, L.; Lee, S.-T.; Jie, J. Organometal Halide Perovskite Quantum Dot Light-Emitting Diodes. *Advanced Functional Materials* **2016**, *26*, 4797–4802.

(35) Møller, C. K. The Structure of Cæsium Plumbo Iodide CsPbI3. *Matematisk-fysiske Meddelelser udgivet af Det Kongelige Danske Videnskabernes Selskab* **1959**, *32*.

(36) Conings, B.; Drijkoningen, J.; Gauquelin, N.; Babayigit, A.; D'Haen, J.; D'Olieslaeger, L.; Ethirajan, A.; Verbeeck, J.; Manca, J.; Mosconi, E.; Angelis, F. D.; Boyen, H.-G. Intrinsic Thermal Instability of Methylammonium Lead Trihalide Perovskite. *Advanced Energy Materials* **2015**, *5*, 1500477.

(37) Cordero, F.; Craciun, F.; Paoletti, A. M.; Zanotti, G. Structural Transitions and Stability of $FAPbI_3$ and $MAPbI_3$: The Role of Interstitial Water. *Nanomaterials* **2021**, *11*, 1610.

(38) Hassan, Y. et al. Ligand-engineered bandgap stability in mixed-halide perovskite LEDs. *Nature* **2021**, *591*, 72–77.

(39) Wells, H. L. ART. XVI.–On the Coesium-and the Potassium-Lead Halides;: Method of Preparation. General Properties. Analytical Methods. the Caesium-Lead Chlorides; by G. F. Campbell. The Caesium-Lead Bromides; by P. T. Walden. The Caesium-Lead Iodide, and some Mixed Double-Halides; by A. P. Wheeler. The Potassium Lead Halides. *American Journal of Science (1880-1910)* **1893**, *45*, 121.

(40) Stoumpos, C. C.; Kanatzidis, M. G. The Renaissance of Halide Perovskites and Their Evolution as Emerging Semiconductors. *Accounts of Chemical Research* **2015**, *48*, 2791–2802.

(41) Protesescu, L.; Yakunin, S.; Bodnarchuk, M. I.; Krieg, F.; Caputo, R.; Hendon, C. H.; Yang, R. X.; Walsh, A.; Kovalenko, M. V. Nanocrystals of Cesium Lead Halide Perovskites ($CsPbX_3$, X = Cl, Br, and I): Novel Optoelectronic Materials Showing Bright Emission with Wide Color Gamut. *Nano Letters* **2015**, *15*, 3692–3696.

(42) Sharma, S.; Weiden, N.; Weiss, A. Phase diagrams of quasibinary systems of the type: ABX_3-$A'BX_3$; ABX_3-$AB'X_3$, and ABX_3-ABX'_3; X = Halogen. *Zeitschrift für Physikalische Chemie* **1992**, *175*, 63–80.

(43) Stoumpos, C. C.; Malliakas, C. D.; Kanatzidis, M. G. Semiconducting Tin and Lead Iodide Perovskites with Organic Cations: Phase Transitions, High Mobilities, and Near-Infrared Photoluminescent Properties. *Inorganic Chemistry* **2013**, *52*, 9019–9038.

(44) Swarnkar, A.; Marshall, A. R.; Sanehira, E. M.; Chernomordik, B. D.; Moore, D. T.; Christians, J. A.; Chakrabarti, T.; Luther, J. M. Quantum dot–induced phase stabilization of α-CsPbI3 perovskite for high-efficiency photovoltaics. *Science* **2016**, *354*, 92–95.

(45) Koh, T. M.; Fu, K.; Fang, Y.; Chen, S.; Sum, T. C.; Mathews, N.; Mhaisalkar, S. G.; Boix, P. P.; Baikie, T. Formamidinium-Containing Metal-Halide: An Alternative Material for Near-IR Absorption Perovskite Solar Cells. *The Journal of Physical Chemistry C* **2014**, *118*, 16458–16462.

(46) Wang, Q.; Jin, Z.; Chen, D.; Bai, D.; Bian, H.; Sun, J.; Zhu, G.; Wang, G.; Liu, S. F. μ-Graphene Crosslinked $CsPbI_3$ Quantum Dots for High Efficiency Solar Cells with Much Improved Stability. *Advanced Energy Materials* **2018**, *8*, 1800007.

(47) Wei, H.; Chen, S.; Zhao, J.; Yu, Z.; Huang, J. Is Formamidinium Always More Stable than Methylammonium? *Chemistry of Materials* **2020**, *32*, 2501–2507.

(48) Qiu, Z.; Li, N.; Huang, Z.; Chen, Q.; Zhou, H. Recent Advances in Improving Phase Stability of Perovskite Solar Cells. *Small Methods* **2020**, *4*, 1900877.

(49) Saliba, M.; Matsui, T.; Domanski, K.; Seo, J.-Y.; Ummadisingu, A.; Zakeeruddin, S. M.; Correa-Baena, J.-P.; Tress, W. R.; Abate, A.; Hagfeldt, A.; Grätzel, M. Incorporation of rubidium cations into perovskite solar cells improves photovoltaic performance. *Science* **2016**, *354*, 206–209.

(50) Turren-Cruz, S.-H.; Hagfeldt, A.; Saliba, M. Methylammonium-free, high-performance, and stable perovskite solar cells on a planar architecture. *Science* **2018**, *362*, 449–453.

(51) Bass, K. K.; McAnally, R. E.; Zhou, S.; Djurovich, P. I.; Thompson, M. E.; Melot, B. C. Influence of moisture on the preparation, crystal structure, and photophysical properties of organohalide perovskites. *Chemical Communications* **2014**, *50*, 15819–15822.

(52) Pathak, S.; Sepe, A.; Sadhanala, A.; Deschler, F.; Haghighirad, A.; Sakai, N.; Goedel, K. C.; Stranks, S. D.; Noel, N.; Price, M.; Hüttner, S.; Hawkins, N. A.; Friend, R. H.; Steiner, U.; Snaith, H. J. Atmospheric Influence upon Crystallization and Electronic Disorder and Its Impact on the Photophysical Properties of Organic–Inorganic Perovskite Solar Cells. *ACS Nano* **2015**, *9*, 2311–2320.

(53) You, J.; Yang, Y. M.; Hong, Z.; Song, T.-B.; Meng, L.; Liu, Y.; Jiang, C.; Zhou, H.; Chang, W.-H.; Li, G.; Yang, Y. Moisture assisted perovskite film growth for high performance solar cells. *Applied Physics Letters* **2014**, *105*, 183902.

(54) Zhou, H.; Chen, Q.; Li, G.; Luo, S.; Song, T.-b.; Duan, H.-S.; Hong, Z.; You, J.; Liu, Y.; Yang, Y. Interface engineering of highly efficient perovskite solar cells. *Science* **2014**, *345*, 542–546.

(55) Huang, H.-H.; Ma, Z.; Strzalka, J.; Ren, Y.; Lin, K.-F.; Wang, L.; Zhou, H.; Jiang, Z.; Chen, W. Mild water intake orients crystal formation imparting high tolerance on unencapsulated halide perovskite solar cells. *Cell Reports Physical Science* **2021**, *2*, 100395.

(56) Eperon, G. E.; Habisreutinger, S. N.; Leijtens, T.; Bruijnaers, B. J.; van Franeker, J. J.; deQuilettes, D. W.; Pathak, S.; Sutton, R. J.; Grancini, G.; Ginger, D. S.; Janssen, R. A. J.; Petrozza, A.; Snaith, H. J. The Importance of Moisture in Hybrid Lead Halide Perovskite Thin Film Fabrication. *ACS Nano* **2015**, *9*, 9380–9393.

(57) Christians, J. A.; Miranda Herrera, P. A.; Kamat, P. V. Transformation of the Excited State and Photovoltaic Efficiency of $CH_3NH_3PbI_3$ Perovskite upon Controlled Exposure to Humidified Air. *Journal of the American Chemical Society* **2015**, *137*, 1530–1538.

(58) Noh, J. H.; Im, S. H.; Heo, J. H.; Mandal, T. N.; Seok, S. I. Chemical Management for Colorful, Efficient, and Stable Inorganic–Organic Hybrid Nanostructured Solar Cells. *Nano Letters* **2013**, *13*, 1764–1769.

(59) Lou, S.; Xuan, T.; Wang, J. (INVITED) Stability: A desiderated problem for the lead halide perovskites. *Optical Materials: X* **2019**, *1*, 100023.

(60) Hintermayr, V.; Lampe, C.; Löw, M.; Roemer, J.; Vanderlinden, W.; Gramlich, M.; Böhm, A. X.; Sattler, C.; Nickel, B.; Lohmueller, T.; Urban, A. S. Polymer nanoreactors shield perovskite nanocrystals from degradation. *Nano Letters* **2019**, acs.nanolett.9b00982.

(61) Li, Z.; Hu, Q.; Tan, Z.; Yang, Y.; Leng, M.; Liu, X.; Ge, C.; Niu, G.; Tang, J. Aqueous Synthesis of Lead Halide Perovskite Nanocrystals with High Water Stability and Bright Photoluminescence. *ACS Applied Materials & Interfaces* **2018**, *10*, 43915–43922.

(62) Boehme, S. C.; Azpiroz, J. M.; Aulin, Y. V.; Grozema, F. C.; Vanmaekelbergh, D.; Siebbeles, L. D.; Infante, I.; Houtepen, A. J. Density of Trap States and Auger-mediated Electron Trapping in CdTe Quantum-Dot Solids. *Nano Letters* **2015**, *15*, 3056–3066.

(63) Jones, M.; Kumar, S.; Lo, S. S.; Scholes, G. D. Exciton Trapping and Recombination in Type II CdSe/CdTe Nanorod Heterostructures. *The Journal of Physical Chemistry C* **2008**, *112*, 5423–5431.

(64) Chestnoy, N.; Harris, T. D.; Hull, R.; Brus, L. E. Luminescence and photophysics of cadmium sulfide semiconductor clusters: the nature of the emitting electronic state. *The Journal of Physical Chemistry* **1986**, *90*, 3393–3399.

(65) Bawendi, M. G.; Carroll, P. J.; Wilson, W. L.; Brus, L. E. Luminescence properties of CdSe quantum crystallites: Resonance between interior and surface localized states. *The Journal of Chemical Physics* **1992**, *96*, 946–954.

(66) Stewart, R. J.; Grieco, C.; Larsen, A. V.; Maier, J. J.; Asbury, J. B. Approaching Bulk Carrier Dynamics in Organo-Halide Perovskite Nanocrystalline Films by Surface Passivation. *The Journal of Physical Chemistry Letters* **2016**, *7*, 1148–1153.

(67) Schmidt, L. C.; Pertegás, A.; González-Carrero, S.; Malinkiewicz, O.; Agouram, S.; Mínguez Espallargas, G.; Bolink, H. J.; Galian, R. E.; Pérez-Prieto, J. Nontemplate Synthesis of CH3NH3PbBr3 Perovskite Nanoparticles. *Journal of the American Chemical Society* **2014**, *136*, 850–853.

(68) Talapin, D. V.; Rogach, A. L.; Kornowski, A.; Haase, M.; Weller, H. Highly Luminescent Monodisperse CdSe and CdSe/ZnS Nanocrystals Synthesized in a Hexadecylamine–Trioctylphosphine Oxide–Trioctylphospine Mixture. *Nano Letters* **2001**, *1*, 207–211.

(69) Green, M. L. H. A new approach to the formal classification of covalent compounds of the elements. *Journal of Organometallic Chemistry* **1995**, *500*, 127–148.

(70) De Roo, J.; Ibáñez, M.; Geiregat, P.; Nedelcu, G.; Walravens, W.; Maes, J.; Martins, J. C.; Van Driessche, I.; Kovalenko, M. V.; Hens, Z. Highly Dynamic Ligand Binding and Light Absorption Coefficient of Cesium Lead Bromide Perovskite Nanocrystals. *ACS Nano* **2016**, *10*, 2071–2081.

(71) Socie, E.; Vale, B. R. C.; Burgos-Caminal, A.; Moser, J.-E. Direct Observation of Shallow Trap States in Thermal Equilibrium with Band-Edge Excitons in Strongly Confined CsPbBr3 Perovskite Nanoplatelets. *Advanced Optical Materials* **2011**, *9*, 2001308.

(72) Hoke, E. T.; Slotcavage, D. J.; Dohner, E. R.; Bowring, A. R.; Karunadasa, H. I.; McGehee, M. D. Reversible photo-induced trap formation in mixed-halide hybrid perovskites for photovoltaics. *Chemical Science* **2015**, *6*, 613–617.

(73) Bischak, C. G.; Hetherington, C. L.; Wu, H.; Aloni, S.; Ogletree, D. F.; Limmer, D. T.; Ginsberg, N. S. Origin of Reversible Photoinduced Phase Separation in Hybrid Perovskites. *Nano Letters* **2017**, *17*, 1028–1033.

(74) Shao, Y.; Fang, Y.; Li, T.; Wang, Q.; Dong, Q.; Deng, Y.; Yuan, Y.; Wei, H.; Wang, M.; Gruverman, A.; Shield, J.; Huang, J. Grain boundary dominated ion migration in polycrystalline organic–inorganic halide perovskite films. *Energy & Environmental Science* **2016**, *9*, 1752–1759.

(75) Sadighian, J. C.; Crawford, M. L.; Suder, T. W.; Wong, C. Y. Surface ligation stage revealed through polarity-dependent fluorescence during perovskite nanocrystal growth. *Journal of Materials Chemistry C* **2020**,

(76) Yang, Y.; Yang, M.; Li, Z.; Crisp, R.; Zhu, K.; Beard, M. C. Comparison of Recombination Dynamics in $CH_3NH_3PbBr_3$ and $CH_3NH_3PbI_3$ Perovskite Films: Influence of Exciton Binding Energy. *The Journal of Physical Chemistry Letters* **2015**, *6*, 4688–4692.

(77) Barker, A. J.; Sadhanala, A.; Deschler, F.; Gandini, M.; Senanayak, S. P.; Pearce, P. M.; Mosconi, E.; Pearson, A. J.; Wu, Y.; Srimath Kandada, A. R.; Leijtens, T.; De Angelis, F.; Dutton, S. E.; Petrozza, A.; Friend, R. H. Defect-Assisted Photoinduced Halide Segregation in Mixed-Halide Perovskite Thin Films. *ACS Energy Letters 2*, 1416–1424.

(78) Yoon, S. J.; Draguta, S.; Manser, J. S.; Sharia, O.; Schneider, W. F.; Kuno, M.; Kamat, P. V. Tracking Iodide and Bromide Ion Segregation in Mixed Halide Lead Perovskites during Photoirradiation. *ACS Energy Letters 1*, 290–296.

(79) Walsh, A.; Scanlon, D. O.; Chen, S.; Gong, X. G.; Wei, S.-H. Self-Regulation Mechanism for Charged Point Defects in Hybrid Halide Perovskites. *Angewandte Chemie* **2015**, *127*, 1811–1814.

(80) Eames, C.; Frost, J. M.; Barnes, P. R. F.; O'Regan, B. C.; Walsh, A.; Islam, M. S. Ionic transport in hybrid lead iodide perovskite solar cells. *Nature Communications* **2015**, *6*, 7497.

(81) Elmelund, T.; Scheidt, R. A.; Seger, B.; Kamat, P. V. Bidirectional Halide Ion Exchange in Paired Lead Halide Perovskite Films with Thermal Activation. *ACS Energy Letters* **2019**, *4*, 1961–1969.

(82) Meggiolaro, D.; Mosconi, E.; De Angelis, F. Formation of Surface Defects Dominates Ion Migration in Lead-Halide Perovskites. *ACS Energy Letters* **2019**, *4*, 779–785.

(83) Motti, S. G.; Meggiolaro, D.; Barker, A. J.; Mosconi, E.; Perini, C. A. R.; Ball, J. M.; Gandini, M.; Kim, M.; De Angelis, F.; Petrozza, A. Controlling competing photochemical reactions stabilizes perovskite solar cells. *Nature Photonics* **2019**, *13*, 532–539.

(84) Belisle, R. A.; Bush, K. A.; Bertoluzzi, L.; Gold-Parker, A.; Toney, M. F.; McGehee, M. D. Impact of Surfaces on Photoinduced Halide Segregation in Mixed-Halide Perovskites. *ACS Energy Letters* **2018**, *3*, 2694–2700.

(85) Chen, W.; Mao, W.; Bach, U.; Jia, B.; Wen, X. Tracking Dynamic Phase Segregation in Mixed-Halide Perovskite Single Crystals under Two-Photon Scanning Laser Illumination. *Small Methods* **2019**, *3*, 1900273.

(86) LaMer, V. K.; Dinegar, R. H. Theory, Production and Mechanism of Formation of Monodispersed Hydrosols. *Journal of the American Chemical Society* **1950**, *72*, 4847–4854.

(87) Wang, F.; Richards, V. N.; Shields, S. P.; Buhro, W. E. Kinetics and Mechanisms of Aggregative Nanocrystal Growth. *Chemistry of Materials 26*, 5–21.

(88) Hassan, Y.; Ashton, O. J.; Park, J. H.; Li, G.; Sakai, N.; Wenger, B.; Haghighirad, A. A.; Noel, N. K.; Song, M. H.; Lee, B. R.; Friend, R. H.; Snaith, H. J. Facile Synthesis of Stable and Highly Luminescent Methylammonium Lead Halide Nanocrystals for Efficient Light Emitting Devices. *Journal of the American Chemical Society* **2019**, *141*, 1269–1279.

(89) Wang, L.; Williams, N. E.; Malachosky, E. W.; Otto, J. P.; Hayes, D.; Wood, R. E.; Guyot-Sionnest, P.; Engel, G. S. Scalable Ligand-Mediated Transport Synthesis of Organic-Inorganic Hybrid Perovskite Nanocrystals with Resolved Electronic Structure and Ultrafast Dynamics. *ACS Nano* **2017**, *11*, 2689–2696.

(90) Wilson, K. S.; Mapile, A. N.; Wong, C. Y. Broadband single-shot transient absorption spectroscopy. *Optics Express* **2020**, *28*, 11339.

(91) Knight, A. J.; Wright, A. D.; Patel, J. B.; McMeekin, D. P.; Snaith, H. J.; Johnston, M. B.; Herz, L. M. Electronic Traps and Phase Segregation in Lead Mixed-Halide Perovskite. *ACS Energy Letters 4*, 75–84.

(92) Crawford, F. S. *Waves*; McGraw-Hill, 1968; Vol. 3.

(93) Tr ager, F., Ed. *Springer Handbook of Lasers and Optics*, 2nd ed.; Springer: New York, 2007; p 1–80.

(94) Alfano, R. R. *The Supercontinuum Laser Source*; Springer New York: New York, NY, 2016.

(95) Couairon, A.; Mysyrowicz, A. Femtosecond filamentation in transparent media. *Physics Reports* **2007**, *441*, 47–189.

(96) Brée, C. *Nonlinear Optics in the Filamentation Regime*; Springer Theses; Springer Berlin Heidelberg: Berlin, Heidelberg, 2012.

(97) Chin, S. L.; Hosseini, S. A.; Liu, W.; Luo, Q.; Thèberge, F.; Ak ozbek, N.; Becker, A.; Kandidov, V. P.; Kosareva, O. G.; Schroeder, H. The propagation of powerful femtosecond laser pulses in opticalmedia: physics, applications, and new challenges. *Canadian Journal of Physics* **2005**, *83*, 863–905.

(98) Dharmadhikari, A. K.; Rajgara, F. A.; Reddy, N. C. S.; Sandhu, A. S.; Mathur, D. Highly efficient white light generation from barium fluoride. *Optics Express* **2004**, *12*, 695.

(99) Wang, J.; Zhang, Y.; Shen, H.; Jiang, Y.; Wang, Z. Spectral stability of supercontinuum generation in condensed mediums. *Optical Engineering* **2017**, *56*, 076107.

(100) Zheng, C.; Mark, M. F.; Wiegand, T.; Diaz, S. A.; Cody, J.; Spano, F. C.; McCamant, D. W.; Collison, C. J. Measurement and Theoretical Interpretation of Exciton Diffusion as a Function of Intermolecular Separation for Squaraines Targeted for Bulk Heterojunction Solar Cells. *The Journal of Physical Chemistry C* **2020**, *124*, 4032–4043.

(101) Queloz, V. I. E.; Bouduban, M. E. F.; García-Benito, I.; Fedorovskiy, A.; Orlandi, S.; Cavazzini, M.; Pozzi, G.; Trivedi, H.; Lupascu, D. C.; Beljonne, D.; Moser, J.-E.; Nazeeruddin, M. K.; Quarti, C.; Grancini, G. Spatial Charge Separation as the Origin of Anomalous Stark Effect in Fluorous 2D Hybrid Perovskites. *Advanced Functional Materials* **2020**, *30*, 2000228.

(102) Klimov, V. I. Spectral and Dynamical Properties of Multiexcitons in Semiconductor Nanocrystals. *Annual Review of Physical Chemistry* **2007**, *58*, 635–673.

(103) Sewall, S. L.; Cooney, R. R.; Anderson, K. E. H.; Dias, E. A.; Sagar, D. M.; Kambhampati, P. State-resolved studies of biexcitons and surface trapping dynamics in semiconductor quantum dots. *The Journal of Chemical Physics* **2008**, *129*, 084701.

(104) Meli, L.; Green, P. F. Aggregation and Coarsening of Ligand-Stabilized Gold Nanoparticles in Poly(methyl methacrylate) Thin Films. *ACS Nano* **2008**, *2*, 1305–1312.

(105) Cheche, T. O.; Barna, V.; Chang, Y.-C. Analytical approach for type-II semiconductor spherical core–shell quantum dots heterostructures with wide band gaps. *Superlattices and Microstructures* **2013**, *60*, 475–486.

(106) Haus, J. W.; Zhou, H. S.; Honma, I.; Komiyama, H. Quantum confinement in semiconductor heterostructure nanometer-size particles. *Physical Review B* **1993**, *47*, 1359–1365.

(107) Li, Y.; Luo, X.; Ding, T.; Lu, X.; Wu, K. Size- and Halide-Dependent Auger Recombination in Lead Halide Perovskite Nanocrystals. *Angewandte Chemie* **2020**, *132*, 14398–14401.

(108) Senno, M.; Tinte, S. Mixed formamidinium–methylammonium lead iodide perovskite from first-principles: hydrogen-bonding impact on the electronic properties. *Physical Chemistry Chemical Physics* **2021**, *23*, 7376–7385.

(109) Zhang, X.; Gharbi, M.; Sharma, P.; Johnson, H. T. Quantum field induced strains in nanostructures and prospects for optical actuation. *International Journal of Solids and Structures* **2009**, *46*, 3810–3824.

(110) Li, Y.; Luo, X.; Ding, T.; Lu, X.; Wu, K. Size- and Halide-Dependent Auger Recombination in Lead Halide Perovskite Nanocrystals. *Angewandte Chemie International Edition* **2020**, *59*, 14292–14295.

(111) Tang, X.; van den Berg, M.; Gu, E.; Horneber, A.; Matt, G. J.; Osvet, A.; Meixner, A. J.; Zhang, D.; Brabec, C. J. Local Observation of Phase Segregation in Mixed-Halide Perovskite. *Nano Letters* **2018**, *18*, 2172–2178.

(112) Mao, W.; Hall, C. R.; Chesman, A. S. R.; Forsyth, C.; Cheng, Y.-B.; Duffy, N. W.; Smith, T. A.; Bach, U. Visualizing Phase Segregation in Mixed-Halide Perovskite Single Crystals. *Angewandte Chemie International Edition* **2019**, *58*, 2893–2898.

(113) Newville, M. et al. *lmfit/lmfit-py: 1.0.3*; Zenodo, 2021.